

# Numerical simulation of borehole acoustic logging in the frequency and time domains with *hp*-adaptive finite elements

Christian Michler<sup>1,2</sup>, Leszek Demkowicz<sup>1</sup>, and Carlos Torres-Verdín<sup>2</sup>

<sup>1</sup>*Institute for Computational Engineering and Sciences (ICES)  
The University of Texas at Austin  
201 East 24th Street, ACES Building  
Austin, Texas 78712, U.S.A.*

<sup>2</sup>*Department of Petroleum and Geosystems Engineering  
The University of Texas at Austin  
1 University Station, Mail Stop C0300  
Austin, Texas 78712, U.S.A.*

*E-mail addresses: c.michler@ices.utexas.edu (C. Michler), leszek@ices.utexas.edu (L. Demkowicz), cverdin@uts.cc.utexas.edu (C. Torres-Verdín)*

---

## Abstract

Accurate numerical simulation of borehole acoustic measurements is of great relevance to improving the efficacy of acoustic logging techniques and to computationally estimating elastic formation properties. Such simulations require sound physical modeling combined with accurate and efficient numerical discretization and solution techniques. The objective of this paper is to concomitantly model acoustic wave propagation in a fluid-filled borehole coupled with elastic wave propagation both in the probed rock formation and in the elastic logging tool. To ensure the accuracy and efficiency of our simulations, we use a self-adaptive finite-element discretization method enhanced with Perfectly-Matched-Layer spatial-domain truncation. This work constitutes the first application of automatic *hp*-adaptivity to a coupled multi-physics problem, which requires the non-trivial capability of propagating refinements between acoustics and elasticity subdomains through their common interface. Computations are carried out in the frequency domain. Subsequently, using an inverse Fourier transform, frequency-domain solutions are transformed into the time domain to obtain waveforms at the receiver positions. Numerical results are presented for monopole and dipole sources with and without the presence of the logging tool, and for a layered formation. To validate our method, we compare our results to published reference data and to results obtained using an in-house finite-difference code. Convergence to a user-specified tolerance for the discretization error confirms the accuracy delivered by our method in the presence of complex geometrical and physical conditions and indicates its potential for the simulation of borehole

acoustic measurements.

*Key words:* acoustic logging, borehole acoustics, wave propagation, linear elasticity, coupled problems, *hp*-adaptive finite elements

---

## 1 Introduction

Acoustic logging is a central component of the non-invasive, in-situ assessment of rock-formation properties in borehole geophysical applications, see e.g. Refs. [17,23,20]. The numerical simulation of problems arising in borehole acoustic logging is of great importance for advancing fundamental knowledge of borehole acoustics and for the improvement of acoustic logging techniques used by oil- and oil-service companies to detect and quantify hydrocarbon-bearing rocks. Moreover, the capability of numerically simulating acoustic logging is a prerequisite for improving data inversion techniques (see e.g. [2,3]), such as the computational estimation of the spatial distribution of elastic formation properties from given borehole acoustic measurements. However, the simulation of borehole acoustic problems poses numerous challenges. First, in general, the computational model needs to be sufficiently sophisticated to capture the essential physics while remaining computationally tractable. Second, the truncation of the unbounded physical domain to a bounded computational domain requires a special treatment of the truncated boundary to avoid non-physical reflections of outward traveling waves. For this purpose the *Perfectly Matched Layer (PML)* technique is commonly employed, see [4]. Third, the accurate resolution of propagating waves requires a sufficiently fine discretization, ideally equipped with some form of estimate of the discretization error.

A review on elastic wave propagation in a fluid-filled borehole has recently been presented in Ref. [6]. Currently available simulation techniques for acoustic logging, such as those presented in [5,12,13,15], are typically based on finite-difference discretizations which are simple and easy to implement. However, finite-difference methods cannot readily provide a measure of the discretization error, and refinements that are locally confined are difficult to implement with finite differences. Moreover, finite-difference methods cannot handle cases of large contrasts of elastic/acoustic properties or of localized wideband diffraction, and they are typically restricted to simple geometries.

To accurately and efficiently simulate borehole acoustic measurements, we use an *hp*-adaptive finite-element method that optimally adapts the discretization in terms of mesh size,  $h$ , and polynomial approximation order,  $p$ , to the local resolution requirements of the solution and delivers a reliable estimate of the discretization error. Starting with a user-specified error tolerance, the adaptivity is carried out *automatically*, i.e. no interaction with the user is necessary,

see [7,8,9]. Such self-adaptive finite-element discretization is ideally suited to meet the above-mentioned challenges in borehole acoustic simulations. In particular, automatic adaptivity in combination with the PML technique is capable of reducing non-physical reflections from spatial domain truncation to an arbitrary level of accuracy, see [14]. However, extending the algorithm for automatic adaptivity to a coupled multi-physics problem requires the capability of propagating refinements between acoustic and elastic subdomains through their common interface which entails a non-trivial challenge.

Our simulations consider a problem setting that is axisymmetric in terms of geometry and media, but allows for sources that are not necessarily axisymmetric. All computations are carried out in the frequency domain. Solving the problem in the frequency domain offers a number of advantages over direct solution in the time domain. In particular, it obviates the stability restriction on the time-step size that is incurred by explicit time-integration methods. Moreover, it allows for the explicit consideration of frequency-dependent material properties such as those due to drilling-induced stress around the borehole. Finally, it enables one to reuse the converged mesh at a given frequency as the initial mesh for the computation at subsequent frequencies, which expedites the adaptivity and provides significant computational savings. We investigate how many frequencies need to be sampled for a sufficiently accurate representation of the time-domain signal. Numerical results are presented for monopole and dipole sources with and without the presence of the logging tool, and for a layered formation. Very good agreement of our results with reference data published in [6] and with results obtained using an in-house finite-difference code confirms the reliability of our method.

The remainder of this paper is organized as follows: In Section 2, we present some preliminaries and techniques that we use to formulate the considered problem, such as the transformation between frequency and time domains, a Fourier series expansion in azimuthal direction and the Perfectly Matched Layer technique. In Section 3, we state the physical problem under consideration and specify the mathematical model used to describe the problem. In Section 4, we concisely review the automatic *hp*-adaptive discretization strategy and briefly elaborate on its extension to multi-physics problems. In Section 5, we conduct numerical simulations of borehole acoustic logging for a monopole and a dipole source, with and without the presence of the tool, and benchmark our results against the data in [6]. In Section 6, we compute acoustic logging for a finite-thickness hard formation shouldered by two soft formations extending to infinity. Finally, in Section 7, we summarize the most important conclusions.

## 2 Mathematical preliminaries to formulate the problem statement

Before presenting the problem statement and governing equations in the next section, we introduce some preliminaries and techniques that provide the framework in which we shall consider the governing equations.

Section 2.1 specifies the transformation between time and frequency domains. Section 2.2 describes a generic formulation of a multipole source exciting the coupled acoustics-elasticity wave propagation. Section 2.3 briefly summarizes the Perfectly Matched Layer technique for reflectionless domain truncation.

### 2.1 Transformation between time and frequency domains

We shall treat the problem in the frequency domain and, thus, assume that the solution can be decomposed into a sum of time-harmonic variations. Let us first formulate the problem for a single frequency and make the following ansatz in time for acoustic pressure  $p$  and elastic displacement  $\mathbf{u}$ :

$$p(\mathbf{x}, t) = \hat{p}(\mathbf{x}, \omega)e^{i\omega t}, \quad (1a)$$

$$\mathbf{u}(\mathbf{x}, t) = \hat{\mathbf{u}}(\mathbf{x}, \omega)e^{i\omega t}, \quad (1b)$$

where  $\mathbf{x}$  and  $t$  denote the vector of space dimensions and time, respectively,  $\omega = 2\pi f$  is the angular frequency with  $f$  denoting the linear frequency, and  $i$  denotes the imaginary unit. The ansatz (1) transforms the time-dependent governing equations into the frequency domain, resulting in an equation system for the complex-valued phasors  $\hat{p}(\mathbf{x}, \omega)$  and  $\hat{\mathbf{u}}(\mathbf{x}, \omega)$ . Computing the solution for “sufficiently many” frequencies, the frequency-domain solutions are then transformed into the time-domain as follows: Considering the inverse Fourier transform for the acoustic pressure

$$p(\mathbf{x}, t) = \frac{1}{2\pi} \int_{-\infty}^{+\infty} \hat{p}(\mathbf{x}, \omega)e^{i\omega t} d\omega \quad (2)$$

for integrands that decay sufficiently fast for  $|\omega|$  large, the integral in (2) can be truncated to a suitable finite interval  $[-\hat{b}, +\hat{b}]$  and thus approximated as

$$p(\mathbf{x}, t) \approx \frac{1}{2\pi} \int_{-\hat{b}}^{+\hat{b}} \hat{p}(\mathbf{x}, \omega)e^{i\omega t} d\omega. \quad (3)$$

The integral in (3) is then evaluated using a numerical integration technique such as the composite trapezoid rule and sampled at discrete, uniformly spaced angular frequencies  $\omega_j$ , i.e. with  $j = 0, \dots, N$ , a constant frequency spacing  $\Delta\omega = 2\hat{b}/N$  and

$$\omega_j = -\hat{b} + j\Delta\omega, \quad j = 0, \dots, N, \quad (4)$$

we approximate (3) as

$$p(\mathbf{x}, t) \approx \frac{1}{2\pi} \left( \frac{\hat{p}(\mathbf{x}, \omega_0)e^{i\omega_0 t} + \hat{p}(\mathbf{x}, \omega_N)e^{i\omega_N t}}{2} + \sum_{j=1}^{N-1} \hat{p}(\mathbf{x}, \omega_j)e^{i\omega_j t} \right) \Delta\omega. \quad (5)$$

The frequency-domain elastic displacement vector can be transformed into its time-domain counterpart in analogy to Eqs. (2)-(5).

Note that relation (5) can alternatively be derived based on the interpretation of the Fourier transform as a limit of the Fourier series; see Ref. [11]. Anticipating a maximum time interval of interest  $[-T, T]$  and replacing the solution in the infinite time domain  $(-\infty, \infty)$  with a periodic extension of the solution in  $[-T, T]$ , we have the Fourier series expansion

$$p(\mathbf{x}, t) = \frac{1}{2\pi} \sum_{k=-\infty}^{\infty} \hat{p}(\mathbf{x}, \omega_k)e^{i\omega_k t} \Delta\omega, \quad (6)$$

where  $\Delta\omega = \pi/T$  and  $\omega_k = k\Delta\omega$ . Note that the frequency spacing  $\Delta\omega$  depends on the anticipated maximum time interval  $T$ . If, for instance, the value of  $T$  doubles, then  $\Delta\omega$  is halved. If the spectrum of the excitation decays with increasing  $|\omega|$ , frequencies that are sufficiently high can be neglected and (6) reduces to (5). In the sequel, we consider the solution in the frequency domain, but shall drop the hat symbol for succinctness.

## 2.2 Modeling of multipole sources

In this subsection, we consider the excitation of the wave propagation by means of a generic multipole source placed in the borehole acoustic fluid. Multipole sources include non-axisymmetric sources, such as the dipole and quadrupole sources for instance, which are typically used to measure the shear-wave velocity of the formation. A dipole source is constructed with a positive displacement of the borehole fluid in one direction and an equal but negative displacement  $180^\circ$  away in azimuth (see Refs. [17, Ch. 6] and [23, Ch. 2]). The resulting radiation pattern of the pressure generated in the borehole exhibits a  $\cos\theta$  dependence, where  $\theta$  is the azimuthal angle. On the other hand, a quadrupole source is constructed with two positive displacements  $180^\circ$  from each other and  $90^\circ$  from the negative displacements. The resulting radiation pattern of the quadrupole source pressure field exhibits a  $\cos 2\theta$  dependence. Thus, a generic multipole source can be described as

$$g_n := p_{\text{ex}} \cos(n\theta), \quad (7)$$

with  $p_{\text{ex}}$  the amplitude of the excitation,  $n$  the azimuthal order number, and the setting  $n = 0, 1, 2$  corresponding to monopole, dipole and quadrupole

sources, respectively<sup>1</sup>. We then rewrite Eq. (7) as

$$g_n = p_{\text{ex}} \frac{e^{+in\theta} + e^{-in\theta}}{2} = \underbrace{p_{\text{ex}} \frac{e^{+in\theta}}{2}}_{g_n^+} + \underbrace{p_{\text{ex}} \frac{e^{-in\theta}}{2}}_{g_n^-}. \quad (8)$$

Writing Eq. (8) in terms of complex exponentials rather than sine and cosine functions enables us to invoke orthogonality arguments that lead to a simplification of the variational statements to be discussed in Section 3.

Due to linearity of the coupled problem, the single-mode multipole source excites only a single solution mode. The acoustics-elasticity solution of azimuthal order  $n$ ,  $(p_n; \mathbf{u}_n)$ , corresponding to the multipole source excitation  $g_n$  exhibits the very same dependence on the angle  $n\theta$  as  $g_n$  and, thus, can be computed by superposing the solutions  $(p_n^+; \mathbf{u}_n^+)$  and  $(p_n^-; \mathbf{u}_n^-)$  of the individual problems excited by  $g_n^+$  and  $g_n^-$ , respectively. Assuming an excitation of the form

$$g_n^+ = p_{\text{ex}} \frac{e^{+in\theta}}{2}, \quad (9)$$

we make the following ansatz for trial solutions  $\mathbf{u}_n, p_n$  and corresponding test functions  $\mathbf{v}_m, q_m$ :

$$\begin{aligned} \mathbf{u}_n^+ &= \tilde{\mathbf{u}}_n(r, z)e^{+in\theta}, & p_n^+ &= \tilde{p}_n(r, z)e^{+in\theta}, \\ \mathbf{v}_m^+ &= \tilde{\mathbf{v}}_m(r, z)e^{+im\theta}, & q_m^+ &= \tilde{q}_m(r, z)e^{+im\theta}, \end{aligned} \quad (10)$$

i.e. trial and test functions with superscript tilde are solely functions of the radial coordinate  $r$  and the axial coordinate  $z$ . Due to orthogonality in both  $L^2$  and  $H^1$  of the exponential ansatz functions in (10), it follows that, upon multiplication of test and trial function in a variational statement, the only non-vanishing contributions are obtained with the setting  $m = -n$ . Note that the negative counterparts of Eqs. (9)-(10) pertaining to  $g_n^-$  are defined accordingly. For succinctness, we shall omit the superscript tilde in the sequel.

For a generic multipole source excitation of the form (9) and corresponding ansatz (10) for test and trial functions, any problem can be treated in a “trace domain”  $\hat{\Omega}$  in the  $(r, z)$ -plane (see also Ref. [9, Ch. 1]) which, for a given azimuthal angle  $\theta^*$ , can be defined implicitly by

$$\Omega = \{(r, \theta^*, z) : (r, z) \in \hat{\Omega}, \theta^* \in [0, 2\pi)\}, \quad (11)$$

with similar assumptions holding for the boundaries  $\Gamma_D$  and  $\Gamma_N$ . As we shall see in Section 3, the variational statements then depend only on the azimuthal

<sup>1</sup> Note that a monopole source ( $n = 0$ ) does not exhibit dependence on the angle of azimuth.

order number  $n$ , with any dependence on the azimuthal angle  $\theta$  being null.

### 2.3 PML formulation in a cylindrical coordinate setting

For problems in borehole acoustic logging the cylindrical coordinate system is the natural choice. The Perfectly Matched Layer formulation of the variational statements that we shall consider in this work can be derived straightforwardly by introducing into the variational statement complex-coordinate stretching in the radial and axial directions according to

$$\begin{aligned} r &\rightarrow R(r, \omega), & \frac{\partial}{\partial r} &\rightarrow \frac{1}{R'} \frac{\partial}{\partial r} & \text{with } R' &= \frac{\partial R}{\partial r}, \\ z &\rightarrow Z(z, \omega), & \frac{\partial}{\partial z} &\rightarrow \frac{1}{Z'} \frac{\partial}{\partial z} & \text{with } Z' &= \frac{\partial Z}{\partial z}, \end{aligned} \quad (12)$$

respectively, stretching of the Jacobian as follows

$$d\Omega = r dr d\theta dz \rightarrow RR'Z' dr d\theta dz = \frac{RR'Z'}{r} d\Omega, \quad (13)$$

and stretching of the line Jacobian  $dS$  accordingly. In Eqs. (12)-(13), for a given angular frequency  $\omega$ ,  $R(r, \omega)$  and  $Z(z, \omega)$  are suitable analytic continuations into the complex plane that are chosen such that the solution in the PML region decays exponentially; see Ref. [14] for details. Denoting by  $r'$  the radial coordinate where the “domain of interest” ends and the PML begins, we have that for a certain  $r^* > r'$  the solution in the PML has decayed to an extent that the PML can be truncated by a homogeneous Dirichlet boundary condition without causing any significant reflections. For a given angular frequency  $\omega$  we specify the analytic continuation of  $R(r, \omega)$  as follows

$$R(r, \omega) = \begin{cases} r & 0 \leq r < r' \\ r + a(r, \omega) - ib(r, \omega) & r \geq r' \end{cases}. \quad (14)$$

Note that, in the domain of interest, such complex-coordinate stretching yields the original real coordinate  $r$  and, accordingly,  $R'$  is equal to unity. By contrast, in the PML the functions  $a(r, \omega)$  and  $b(r, \omega)$  are defined such that the redefined coordinate has additional real and imaginary parts that accelerate the decay of evanescent and propagating waves, respectively. Functions  $a(r, \omega)$  and  $b(r, \omega)$  are typically set to increase steadily from zero as one moves away from the interface  $r'$  into the PML region. We specify the functions  $a(r, \omega)$  and  $b(r, \omega)$  that we use for our numerical experiments in Section 5 and refer for details to Ref. [14]. Note that  $Z(z, \omega)$  can be defined analogously to Eq. (14).

### 3 Problem statement and governing equations

In this section, we specify the mathematical models used to describe acoustic wave propagation in the borehole fluid coupled with elastic wave propagation in the formation and the logging tool. Specifying the governing variational equations based on the preliminaries and techniques presented in Section 2, the problem is treated in the frequency domain and excited with a multipole source. The latter strategy allows us to treat the equations in a generic form, encompassing monopole, dipole and quadrupole sources. As a special case of this generic form we then consider more closely the excitation with a monopole source that yields a two-dimensional axisymmetric solution. By contrast, dipole and quadrupole sources yield a solution that is not axisymmetric. However, the geometry of the problem and, therefore, the domain and its boundaries are assumed to be axisymmetric throughout. Finally, we will present the PML formulation of the governing variational equations which extends the equations from the physical domain into the PML region.

Sections 3.1, 3.2 and 3.3 specify the governing equations for linear acoustics, linear elasticity and the interface conditions, respectively. Based thereon, Section 3.4 summarizes the system of coupled acoustics-elasticity equations.

#### 3.1 Linear acoustics equation

Acoustic wave propagation in the borehole fluid is described by the Helmholtz equation for the acoustic pressure

$$-\Delta p - k^2 p = 0, \quad (15)$$

where  $\Delta$  denotes the Laplacian operator and  $k := \omega/c$  is the wavenumber with  $c$  the sound speed in the fluid. Eq. (15) originates from a system of first-order equations and, for deriving the variational formulation, it is more illuminating to start from this first-order system than from Eq. (15), as we shall see in the sequel. The classical linear acoustics equations are obtained by linearizing the isentropic form of the compressible Euler equations around the hydrostatic equilibrium state (see for instance Ref. [10]), which yields the linearized continuity and momentum equations

$$\begin{cases} i\omega p + \rho_{f,0} c^2 \nabla \cdot \mathbf{v} = 0 \\ i\omega \rho_{f,0} \mathbf{v} + \nabla p = \mathbf{0}, \end{cases} \quad (16)$$

respectively, where  $\mathbf{v}$  denotes the perturbation in velocity of a uniform stationary fluid, and  $\rho_{f,0}$  is the fluid density associated with this uniform state.

Upon eliminating the velocity from the first-order system (16), the Helmholtz equation (15) is obtained.

The variational formulation in terms of pressure is obtained by multiplying Eq. (16)<sub>1</sub> with a test function  $q$ , integrating it over the acoustics subdomain  $\Omega_A$  and integrating the second term by parts which yields

$$\begin{cases} p \in p_D + \mathcal{Q} \\ \int_{\Omega_A} (i\omega pq - \rho_{f,0}c^2 \mathbf{v} \cdot \nabla q) d\Omega = -\rho_{f,0}c^2 \int_{\Gamma_{N,A}} \mathbf{v} \cdot \mathbf{n} q dS \\ \forall q \in \mathcal{Q}, \end{cases} \quad (17)$$

where  $p_D$  denotes a finite-energy lift of the Dirichlet data and  $\mathcal{Q}$  is the space of test functions defined as

$$\mathcal{Q} := \{q \in \mathcal{X} : q = 0 \text{ on } \Gamma_{D,A}\}, \quad (18)$$

and the “energy space”  $\mathcal{X}$  associated with the variational problem (17) is defined as

$$\mathcal{X} := \left\{ q : q, (\nabla q)_l \in L^2(\Omega_A) \right\} \quad l = 1, \dots, d. \quad (19)$$

Multiplying Eq. (17) with  $i\omega$  and eliminating velocity through substitution of Eq. (16)<sub>2</sub> yields the variational formulation

$$\begin{cases} p \in p_D + \mathcal{Q} \\ \int_{\Omega_A} (\nabla p \cdot \nabla q - k^2 pq) d\Omega = \int_{\Gamma_{N,A}} \nabla p \cdot \mathbf{n} q dS \\ \forall q \in \mathcal{Q}. \end{cases} \quad (20)$$

Note that in deriving the variational formulation (20), we have treated the continuity equation in a weak, i.e. variational, sense, whereas the momentum equations have been treated in the strong sense which implies that they are satisfied pointwise. Obviously, Eq. (20) is the variational formulation of the second-order Helmholtz equation (15), but it has been derived without actually invoking (15).

Eq. (20) is then supplemented with additional boundary conditions. To this end, let us subdivide the Neumann boundary  $\Gamma_{N,A}$  into two disjoint subsets

on which boundary conditions are imposed as follows:

$$\begin{aligned} \nabla p \cdot \mathbf{n} &= g_{A,ex} & \text{on } \Gamma_{N,A,ex}, \\ \nabla p \cdot \mathbf{n} &= g_{AE} & \text{on } \Gamma_I. \end{aligned} \quad (21)$$

In the equations above,  $\Gamma_{N,A,ex}$  denotes the part of the Neumann boundary on which a prescribed excitation  $g_{A,ex}$  is applied<sup>2</sup>, whereas  $\Gamma_I$  denotes the interface between acoustics and elasticity subdomains, and  $g_{AE}$  is then specified by interface conditions which we describe in Section 3.3. Inserting the boundary conditions given by (21) into Eq. (20), we obtain

$$\left\{ \begin{array}{l} p \in p_D + \mathcal{Q} \\ \int_{\Omega_A} (\nabla p \cdot \nabla q - k^2 pq) d\Omega = \int_{\Gamma_{N,A,ex}} g_{A,ex} q dS + \int_{\Gamma_I} g_{AE} q dS \\ \forall q \in \mathcal{Q}. \end{array} \right. \quad (22)$$

The acoustics subproblem is specified on a subdomain  $\Omega_A$  that, in radial direction  $r$ , is bounded by the interface  $\Gamma_I$  with the elasticity subdomain (see also the sketch of the problem setting in Fig. 1), which requires the specification of interface conditions; see Section 3.3. In vertical direction  $z$ , the acoustics subdomain  $\Omega_A$  is unbounded, which requires the specification of the Sommerfeld radiation condition at infinity

$$\frac{\partial p}{\partial \zeta} + ikp \in L^2(\Omega_A), \quad (23)$$

where  $\zeta$  denotes the radius in a spherical coordinate system. Eq. (23) allows for outgoing waves only while eliminating unphysical solutions that correspond to waves coming in from infinity. We remark that this particular form of Sommerfeld's radiation condition has the advantage of being independent of the number of space dimensions.

The Sommerfeld radiation condition is effectively implemented by reflectionless truncation of the acoustics domain by a Perfectly Matched Layer which allows for outgoing waves only. Under PML complex-coordinate stretching

<sup>2</sup> According to (16)<sub>2</sub>, such boundary condition is equivalent to a prescribed normal velocity and can be realized, e.g., by the action of a movable cylinder; see [17, Ch. 6].

according to Eqs. (12)-(13), the variational statement (22) translates into

$$\left\{ \begin{array}{l} p \in p_D + \tilde{\mathcal{Q}} \\ \int_{\Omega_A} \frac{RR'Z'}{r} (\tilde{\nabla}p \cdot \tilde{\nabla}q - k^2pq) d\Omega = \int_{\Gamma_{N,A,ex}} \frac{RR'Z'}{r} g_{A,ex} q dS \\ \qquad \qquad \qquad + \int_{\Gamma_I} \frac{RR'Z'}{r} g_{AE} q dS \quad \forall q \in \tilde{\mathcal{Q}}, \end{array} \right. \quad (24)$$

where the stretched gradient operator in cylindrical coordinates is defined as follows

$$\tilde{\nabla}p = \frac{1}{R'} \frac{\partial p}{\partial r} \mathbf{e}_r + \frac{1}{R} \frac{\partial p}{\partial \theta} \mathbf{e}_\theta + \frac{1}{Z'} \frac{\partial p}{\partial z} \mathbf{e}_z, \quad (25)$$

where  $\mathbf{e}_i$  denotes the unit vector in the respective directions. Note that we shall drop the superscript tilde pertaining to the stretched counterparts from the gradient operator and the space of test functions in the sequel. Upon introducing the ansatz (10) for expanding the solution in terms of the azimuthal angle with  $n$  denoting the azimuthal order number, we rewrite Eq. (25) as

$$\nabla p = \left( \frac{1}{R'} \frac{\partial p_n}{\partial r} \mathbf{e}_r + \frac{1}{R} i n p_n \mathbf{e}_\theta + \frac{1}{Z'} \frac{\partial p_n}{\partial z} \mathbf{e}_z \right) e^{in\theta}. \quad (26)$$

Given that the corresponding expression for  $\nabla q$  is similar to the equation above but with azimuthal order  $m$  instead of  $n$  for the test function according to Eq. (10), non-zero contributions in Eq. (24) are obtained only for  $m = -n$ . In the sequel, we suppress the subscripts  $n$  and  $m$  pertaining to the azimuthal order. In accordance with the complex-coordinate stretching carried out above, the space of test functions  $\mathcal{Q}$  needs to be redefined as follows

$$\mathcal{Q} := \{q \in \mathcal{X} : q = 0 \text{ on } \hat{\Gamma}_{D,A}\}, \quad (27)$$

and the “energy space”  $\mathcal{X}$  associated with the variational problem (24) is defined as

$$\mathcal{X} := \left\{ q : \left| \frac{RR'Z'}{r} \right|^{\frac{1}{2}} q, \left| \frac{RZ'}{r} \right|^{\frac{1}{2}} \frac{\partial q}{\partial r}, \left| \frac{R'Z'}{r} \right|^{\frac{1}{2}} q, \left| \frac{RR'}{r} \right|^{\frac{1}{2}} \frac{\partial q}{\partial z} \in L^2(\hat{\Omega}_A) \right\}. \quad (28)$$

In Eqs. (27) and (28),  $\hat{\Gamma}_{D,A}$  and  $\hat{\Omega}_A$  refer to the boundary trace and trace domain corresponding to  $\Gamma_{D,A}$  and  $\Omega_A$ , respectively, as specified in Eq. (11).

For latter use, we identify the bilinear and linear forms pertaining to the

variational statement (24) as

$$b(q, p) = \int_{\hat{\Omega}_A} \frac{RR'Z'}{r} (\nabla p \cdot \nabla q - k^2 pq) d\Omega, \quad (29a)$$

$$l(q) = \int_{\hat{\Gamma}_{N,A,ex}} \frac{RR'Z'}{r} g_{A,ex} q dS + \int_{\hat{\Gamma}_I} \frac{RR'Z'}{r} g_{AE} q dS. \quad (29b)$$

### 3.2 Linear elasticity equations

Elastic wave propagation in the formation surrounding the borehole and in the measurement tool is described by the equations of linear elasticity. Let us recall the equations of linear elasticity in  $\mathbb{R}^d$  and time-harmonic form, which are given by the balance of linear momentum, the constitutive law and the Cauchy displacement-strain relation, respectively, viz.

$$\begin{cases} -\sigma_{ij,j} - \rho_s \omega^2 u_i = 0 & i = 1, \dots, d \\ \sigma_{ij} = E_{ijkl} \epsilon_{kl} & i, j = 1, \dots, d \\ \epsilon_{kl} = \frac{1}{2}(u_{k,l} + u_{l,k}) & k, l = 1, \dots, d, \end{cases} \quad (30)$$

where in the equation above and throughout this section we make use of the Einstein summation convention;  $u_i$  denotes the  $i$ -th component of the displacement vector,  $\sigma_{ij}$  and  $\epsilon_{kl}$  are the components of the stress tensor and of the strain tensor, respectively,  $\rho_s$  is the density of the solid under consideration (formation or tool) and  $E_{ijkl}$  are the components of the elasticity tensor satisfying the usual symmetry properties

$$E_{ijkl} = E_{jikl}, \quad E_{ijkl} = E_{ijlk}, \quad \text{and} \quad E_{ijkl} = E_{klij}. \quad (31)$$

The second symmetry property in (31) implies for Eqs. (30)<sub>2</sub> and (30)<sub>3</sub> that

$$\sigma_{ij} = E_{ijkl} \epsilon_{kl} = E_{ijkl} \frac{1}{2}(u_{k,l} + u_{l,k}) = E_{ijkl} u_{k,l}. \quad (32)$$

For an isotropic homogeneous material, the elasticity tensor depends on two constants only, viz.

$$E_{ijkl} = \mu(\delta_{ik}\delta_{jl} + \delta_{il}\delta_{jk}) + \lambda\delta_{ij}\delta_{kl}, \quad (33)$$

in which case the constitutive law (30)<sub>2</sub> reduces to

$$\sigma_{ij} = 2\mu\epsilon_{ij} + \lambda\epsilon_{kk}\delta_{ij}, \quad (34)$$

where  $\mu$  and  $\lambda$  are the Lamé constants and  $\delta_{ij}$  is the Kronecker delta.

The system of equations (30) can be complemented by various boundary conditions of which we shall restrict ourselves to the simplest ones:

$$u_i = 0, \quad i = 1, \dots, d \quad \text{on } \Gamma_{D,E}, \quad (35a)$$

$$t_i := \sigma_{ij}n_j = g_{EA,i}, \quad i = 1, \dots, d \quad \text{on } \Gamma_{N,E}, \quad (35b)$$

where  $n_j$  are the components of the outward normal unit vector, and  $t_i = g_{EA,i}$  are prescribed tractions. Eq. (35a) prescribes zero displacements and corresponds to homogeneous Dirichlet boundary conditions (as applied at the PML boundary), whereas Eq. (35b) prescribes given tractions and corresponds to Neumann boundary conditions (as applied at the fluid-solid interface  $\Gamma_I$  which, here, is identical to  $\Gamma_{N,E}$ ; see Section 3.3).

To derive the standard variational formulation in terms of the displacement vector, we multiply the momentum equations (30)<sub>1</sub> with a test function  $\mathbf{v} := v_i \in \mathcal{V}$ , integrate over the elasticity subdomain  $\Omega_E$  and, upon integration-by-parts, we obtain

$$\left\{ \begin{array}{l} \mathbf{u} \in \mathcal{V} \\ \int_{\Omega_E} \sigma_{ij}v_{i,j} d\Omega - \int_{\Gamma_{N,E}} \sigma_{ij}n_jv_i dS - \omega^2 \int_{\Omega_E} \rho_s u_i v_i d\Omega = 0, \\ \forall \mathbf{v} \in \mathcal{V}, \end{array} \right. \quad (36)$$

where  $\mathcal{V}$  is the space of test functions

$$\mathcal{V} := \{\mathbf{v} \in \mathcal{X} : \mathbf{v} = \mathbf{0} \text{ on } \Gamma_{D,E}\}, \quad (37)$$

which constitutes a subspace of the energy space  $\mathcal{X} := \mathbf{H}^1(\Omega_E) := (H^1(\Omega_E))^d$ . Substitution of the Neumann boundary condition (35b) into Eq. (36), and noting that in (36) the stress tensor  $\sigma_{ij}(\mathbf{u}) = E_{ijkl} \epsilon_{kl}(\mathbf{u})$  is symmetric and, thus, “sees” only the symmetric part of the tensor  $v_{i,j}$ , that is  $\frac{1}{2}(v_{i,j} + v_{j,i}) = \epsilon_{ij}(\mathbf{v})$ , the variational statement (36) can also be written as

$$\left\{ \begin{array}{l} \mathbf{u} \in \mathcal{V} \\ \int_{\Omega_E} E_{ijkl} \epsilon_{kl}(\mathbf{u}) \epsilon_{ij}(\mathbf{v}) d\Omega - \omega^2 \int_{\Omega_E} \rho_s u_i v_i d\Omega = \int_{\Gamma_I} g_{EA,i} v_i dS, \\ \forall \mathbf{v} \in \mathcal{V}. \end{array} \right. \quad (38)$$

The bilinear and linear forms in accordance with (38) are, respectively,

$$b(\mathbf{v}, \mathbf{u}) = \int_{\Omega_E} E_{ijkl} \epsilon_{kl}(\mathbf{u}) \epsilon_{ij}(\mathbf{v}) d\Omega - \omega^2 \int_{\Omega_E} \rho_s \mathbf{u} \cdot \mathbf{v} d\Omega \quad (39a)$$

$$l(\mathbf{v}) = \int_{\Gamma_I} g_{EA,i} v_i dS. \quad (39b)$$

To express the variational formulation (38) in cylindrical coordinates, we make use of Eq. (39a) and, to this end, recall the formulas for the strain tensor  $\epsilon_{kl}(\mathbf{u}) = \frac{1}{2}(u_{k,l} + u_{l,k})$  in cylindrical coordinates:

$$\epsilon_{rr}(\mathbf{u}) = \frac{\partial u_r}{\partial r}, \quad (40a)$$

$$\epsilon_{\theta\theta}(\mathbf{u}) = \frac{1}{r} \left( \frac{\partial u_\theta}{\partial \theta} + u_r \right), \quad (40b)$$

$$\epsilon_{zz}(\mathbf{u}) = \frac{\partial u_z}{\partial z}, \quad (40c)$$

$$\epsilon_{r\theta}(\mathbf{u}) = \frac{1}{2} \left( \frac{\partial u_\theta}{\partial r} + \frac{1}{r} \left( \frac{\partial u_r}{\partial \theta} - u_\theta \right) \right), \quad (40d)$$

$$\epsilon_{rz}(\mathbf{u}) = \frac{1}{2} \left( \frac{\partial u_z}{\partial r} + \frac{\partial u_r}{\partial z} \right), \quad (40e)$$

$$\epsilon_{\theta z}(\mathbf{u}) = \frac{1}{2} \left( \frac{1}{r} \frac{\partial u_z}{\partial \theta} + \frac{\partial u_\theta}{\partial z} \right). \quad (40f)$$

Upon introducing the ansatz (10) for expanding the solution in terms of the azimuthal angle with  $n$  denoting the azimuthal order number and PML complex-coordinate stretching according to (12), we rewrite Eq. (40) as

$$\epsilon_{rr}(\mathbf{u}) = \frac{1}{R'} \frac{\partial u_{r,n}}{\partial r} e^{in\theta}, \quad (41a)$$

$$\epsilon_{\theta\theta}(\mathbf{u}) = \frac{1}{R} (inu_{\theta,n} + u_{r,n}) e^{in\theta}, \quad (41b)$$

$$\epsilon_{zz}(\mathbf{u}) = \frac{1}{Z'} \frac{\partial u_{z,n}}{\partial z} e^{in\theta}, \quad (41c)$$

$$\epsilon_{r\theta}(\mathbf{u}) = \frac{1}{2} \left( \frac{1}{R'} \frac{\partial u_{\theta,n}}{\partial r} + \frac{1}{R} (inu_{r,n} - u_{\theta,n}) \right) e^{in\theta}, \quad (41d)$$

$$\epsilon_{rz}(\mathbf{u}) = \frac{1}{2} \left( \frac{1}{R'} \frac{\partial u_{z,n}}{\partial r} + \frac{1}{Z'} \frac{\partial u_{r,n}}{\partial z} \right) e^{in\theta}, \quad (41e)$$

$$\epsilon_{\theta z}(\mathbf{u}) = \frac{1}{2} \left( \frac{1}{R} inu_{z,n} + \frac{1}{Z'} \frac{\partial u_{\theta,n}}{\partial z} \right) e^{in\theta}. \quad (41f)$$

Note that  $\epsilon(\mathbf{v})$  is defined accordingly with the ansatz for test functions given

in (10). As mentioned under (10), due to orthogonality of the complex exponential ansatz functions, the only non-vanishing contributions to the variational statement under consideration are obtained with the setting  $m = -n$ .

With the definitions in (41) and stretching of the Jacobian as given in (13), we express the bilinear form (39a) in cylindrical coordinates, with PML complex-coordinate stretching and for a generic azimuthal order  $n$  as

$$\begin{aligned}
b(\mathbf{v}, \mathbf{u}) = & \int_{\Omega_E} \frac{RR'Z'}{r} \left( 2\mu \left[ \epsilon_{rr}(\mathbf{u})\epsilon_{rr}(\mathbf{v}) + \epsilon_{\theta\theta}(\mathbf{u})\epsilon_{\theta\theta}(\mathbf{v}) + \epsilon_{zz}(\mathbf{u})\epsilon_{zz}(\mathbf{v}) \right. \right. \\
& \left. \left. + 2\epsilon_{r\theta}(\mathbf{u})\epsilon_{r\theta}(\mathbf{v}) + 2\epsilon_{rz}(\mathbf{u})\epsilon_{rz}(\mathbf{v}) + 2\epsilon_{\theta z}(\mathbf{u})\epsilon_{\theta z}(\mathbf{v}) \right] \right. \\
& \left. + \lambda \left[ \epsilon_{rr}(\mathbf{u}) + \epsilon_{\theta\theta}(\mathbf{u}) + \epsilon_{zz}(\mathbf{u}) \right] \left[ \epsilon_{rr}(\mathbf{v}) + \epsilon_{\theta\theta}(\mathbf{v}) + \epsilon_{zz}(\mathbf{v}) \right] \right) r dr d\theta dz \\
& - \omega^2 \int_{\Omega_E} \frac{RR'Z'}{r} \rho_s \left[ u_r v_r + u_\theta v_\theta + u_z v_z \right] r dr d\theta dz. \quad (42a)
\end{aligned}$$

Accordingly, the linear form is expressed as

$$l(\mathbf{v}) = \int_{\Gamma_I} \frac{RR'Z'}{r} \left[ g_{EA,r} v_r + g_{EA,\theta} v_\theta + g_{EA,z} v_z \right] dS. \quad (42b)$$

Under PML complex-coordinate stretching and for a generic azimuthal order, the space of test and trial functions is the energy space corresponding to the variational form (42), which is essentially a weighted  $\mathbf{H}^1$  space with weights incorporating the stretching functions and their derivatives; see Ref. [14] for details.

Eq. (42) gives the variational formulation for a multipole source of azimuthal order  $n$ , encompassing a monopole ( $n = 0$ ), a dipole ( $n = 1$ ) and a quadrupole ( $n = 2$ ) source. In the case of a monopole, the problem is axisymmetric and can be fully described by considering it in a “trace domain”  $\tilde{\Omega}$  in the  $(r, z)$ -plane as defined in Eq. (11). Since in the axisymmetric case all unknowns are independent of  $\theta$ , the bilinear form separates into two terms, viz. one that is dependent on the  $r$  and  $z$  components, and the other one that depends on the  $\theta$  component only, namely,

$$b((v_r, v_\theta, v_z), (u_r, u_\theta, u_z)) = b_1((v_r, v_z), (u_r, u_z)) + b_2(v_\theta, u_\theta), \quad (43)$$

and a similar decomposition holds for the linear form  $l(\mathbf{v})$ . Testing with  $v_\theta$ , namely,

$$b((0, v_\theta, 0), (u_r, u_\theta, u_z)) = b_2(v_\theta, u_\theta) = l(0, v_\theta, 0) \quad \forall v_\theta \quad (44)$$

yields a decoupled boundary-value problem for the  $u_\theta$  component. For a monopole source, the loading assumptions imply that  $u_\theta = 0$ , in which case the solu-

tion reduces to determining the  $u_r, u_z$  components only. The formulas for the bilinear and linear forms given in Eq. (42) then simplify to

$$\begin{aligned}
b(\mathbf{v}, \mathbf{u}) = & \int_{\hat{\Omega}_E} \frac{RR'Z'}{r} \left( 2\mu \left[ \epsilon_{rr}(\mathbf{u})\epsilon_{rr}(\mathbf{v}) + \epsilon_{\theta\theta}(\mathbf{u})\epsilon_{\theta\theta}(\mathbf{v}) + \epsilon_{zz}(\mathbf{u})\epsilon_{zz}(\mathbf{v}) \right. \right. \\
& \left. \left. + 2\epsilon_{rz}(\mathbf{u})\epsilon_{rz}(\mathbf{v}) \right] \right. \\
& \left. + \lambda \left[ \epsilon_{rr}(\mathbf{u}) + \epsilon_{\theta\theta}(\mathbf{u}) + \epsilon_{zz}(\mathbf{u}) \right] \left[ \epsilon_{rr}(\mathbf{v}) + \epsilon_{\theta\theta}(\mathbf{v}) + \epsilon_{zz}(\mathbf{v}) \right] \right) r dr dz \\
& - \omega^2 \int_{\hat{\Omega}_E} \frac{RR'Z'}{r} \rho_s \left[ u_r v_r + u_z v_z \right] r dr dz, \quad (45a)
\end{aligned}$$

$$l(\mathbf{v}) = \int_{\hat{\Gamma}_I} \frac{RR'Z'}{r} \left[ g_{EA,r} v_r + g_{EA,z} v_z \right] r dr dz, \quad (45b)$$

where

$$\epsilon_{rr}(\mathbf{u}) = \frac{1}{R'} \frac{\partial u_r}{\partial r}, \quad (46a)$$

$$\epsilon_{\theta\theta}(\mathbf{u}) = \frac{1}{R} u_r, \quad (46b)$$

$$\epsilon_{zz}(\mathbf{u}) = \frac{1}{Z'} \frac{\partial u_z}{\partial z}, \quad (46c)$$

$$\epsilon_{rz}(\mathbf{u}) = \frac{1}{2} \left( \frac{1}{R'} \frac{\partial u_z}{\partial r} + \frac{1}{Z'} \frac{\partial u_r}{\partial z} \right). \quad (46d)$$

Note that, since for the axisymmetric case there is no dependence of the variational statement on the azimuthal angle  $\theta$ , the integration over  $\theta$  actually yields a factor of  $2\pi$  in front of each volume and boundary integral. Since this factor arises consistently in each integral, we have cancelled it out from the variational statement (45).

Let us point out that also for a generic multipole source the problem can be treated in a trace domain in the  $(r, z)$ -plane although the solution is not axisymmetric but depends on the azimuthal angle according to ansatz (10). In this case, the variational statement as given by the bilinear and linear forms in (42) with the definition of the strain tensor in (41) depends on the azimuthal order number  $n$ , but any dependence on the azimuthal angle  $\theta$  is null. Therefore, in the sequel, we shall drop the superscript hat from the domain and boundary symbols with the understanding that the problem is considered in such a trace domain.

Finally, we remark that, for an elasticity problem that is set in a cylindrical coordinate system, finite-energy conditions need in principle to be imposed at radius  $r = 0$  to cope with the singularity arising from the  $1/r$ -factor in the

definition of the strain tensor, Eq. (40). Such finite-energy conditions are conceptually the same as the ones given in Ref. [18] for electromagnetics; however, the precise form of these conditions depends on the underlying physics.

### 3.3 Conditions at the fluid-solid interface

The conditions at the fluid-solid interface state the compatibility of displacements and tractions at the interface. To present these interface conditions in their most convenient form, let us first carry out some straightforward manipulations. The compatibility of displacements translates into the compatibility of velocities at the interface and, for an inviscid fluid which does not support shear, into the compatibility of normal velocity components, viz.

$$\mathbf{v}_f \cdot \mathbf{n}_f = i\omega \mathbf{u}_s \cdot \mathbf{n}_f, \quad (47)$$

where  $\mathbf{v}_f$  denotes the acoustic fluid velocity,  $i\omega \mathbf{u}_s$  corresponds to the velocity of the solid expressed in the frequency domain with  $\mathbf{u}_s$  the displacement vector, and  $\mathbf{n}_f$  is the fluid unit outward normal. Using Eq. (16)<sub>2</sub> to express the acoustic velocity in (47) in terms of the pressure gradient, and recalling the definition (35b) of the traction for elasticity, we can write the conditions at the fluid-solid interface  $\Gamma_I$  as

$$\begin{aligned} g_{AE} &= \nabla p \cdot \mathbf{n}_f = \rho_{f,0} \omega^2 \mathbf{u}_s \cdot \mathbf{n}_f, \\ \mathbf{g}_{EA} &= \boldsymbol{\sigma} \cdot \mathbf{n}_s = -p \mathbf{n}_s, \end{aligned} \quad (48)$$

where  $\mathbf{n}_s$  is the unit outward normal of the solid subdomain. Eq. (48)<sub>1</sub> relates the acoustic pressure gradient in the normal direction to the normal displacement of the solid, and Eq. (48)<sub>2</sub> specifies that the normal traction of the solid is in equilibrium with the fluid pressure and that the fluid does not support any shear forces.

### 3.4 System of coupled acoustics-elasticity equations

Below, we establish the system of coupled acoustics-elasticity equations. Upon substituting the interface conditions (48)<sub>1</sub> and (48)<sub>2</sub> into Eqs. (29b) and (42b), respectively, the boundary terms (29b) and (42b) translate into the bilinear forms (49b) and (49c) below that express the coupling between acoustics and elasticity subsystems. Mind that the transition from the linear forms (29b) and (42b) to the bilinear forms (49b) and (49c) involves a sign change, since the bilinear forms are associated with the left-hand-side of the equations. Note that the linear form (29b) actually comprises two parts; the integral over the

acoustics Neumann boundary,  $\Gamma_{N,A,ex}$ , provides the excitation that drives the coupled system (Eq. (49e) below), whereas the integral over the interface,  $\Gamma_I$ , translates into the coupling term (49b). In addition to the coupling terms, we also recall the bilinear forms associated with the acoustics and elasticity interior domains, Eqs. (29a) and (42a), respectively, so that we can write the coupled acoustics-elasticity system collectively as

$$b_{AA}(q, p) = \int_{\Omega_A} \frac{RR'Z'}{r} (\nabla p \cdot \nabla q - k^2 pq) r dr dz, \quad (49a)$$

$$b_{AE}(q, \mathbf{u}) = - \int_{\Gamma_I} \frac{RR'Z'}{r} (\rho_{f,0} \omega^2 \mathbf{u}_s \cdot \mathbf{n}_f) q dS, \quad (49b)$$

$$b_{EA}(\mathbf{v}, p) = \int_{\Gamma_I} \frac{RR'Z'}{r} (p \mathbf{v} \cdot \mathbf{n}_s) dS, \quad (49c)$$

$$\begin{aligned} b_{EE}(\mathbf{v}, \mathbf{u}) = & \int_{\Omega_E} \frac{RR'Z'}{r} \left( 2\mu \left[ \epsilon_{rr}(\mathbf{u}) \epsilon_{rr}(\mathbf{v}) + \epsilon_{\theta\theta}(\mathbf{u}) \epsilon_{\theta\theta}(\mathbf{v}) + \epsilon_{zz}(\mathbf{u}) \epsilon_{zz}(\mathbf{v}) \right. \right. \\ & \left. \left. + 2\epsilon_{r\theta}(\mathbf{u}) \epsilon_{r\theta}(\mathbf{v}) + 2\epsilon_{rz}(\mathbf{u}) \epsilon_{rz}(\mathbf{v}) + 2\epsilon_{\theta z}(\mathbf{u}) \epsilon_{\theta z}(\mathbf{v}) \right] \right. \\ & \left. + \lambda \left[ \epsilon_{rr}(\mathbf{u}) + \epsilon_{\theta\theta}(\mathbf{u}) + \epsilon_{zz}(\mathbf{u}) \right] \left[ \epsilon_{rr}(\mathbf{v}) + \epsilon_{\theta\theta}(\mathbf{v}) + \epsilon_{zz}(\mathbf{v}) \right] \right) r dr dz \\ & - \omega^2 \int_{\Omega_E} \frac{RR'Z'}{r} \rho_s \left[ u_r v_r + u_\theta v_\theta + u_z v_z \right] r dr dz, \quad (49d) \end{aligned}$$

$$l(q) = \int_{\Gamma_{N,A,ex}} \frac{RR'Z'}{r} g_{A,ex} q dS, \quad (49e)$$

where the line Jacobian  $dS$  equals  $r dr$  or  $r dz$  depending on the orientation of the boundary. Invoking  $\mathbf{n}_s = -\mathbf{n}_f$  and a suitable rescaling of the coupling terms  $b_{AE}(q, \mathbf{u})$  and  $b_{EA}(\mathbf{v}, p)$  leads to a coupled acoustics-elasticity system that is symmetric. Moreover, note that the system (49) is in fact specified for a generic azimuthal order  $n$ ; however, to avoid proliferation of super- and subscripts, we have suppressed the subscript  $n$  from test and trial functions.

Regarding the coupling terms (49b) and (49c), note that the primary variable of one subsystem constitutes the flux for the other subsystem. In particular, the pressure as the primary variable of the acoustic subsystem constitutes the flux for the elastic subsystem, viz. the tractions. Conversely, the displacement vector as the primary variable of the elastic subsystem provides the flux for the acoustic subsystem, viz. the normal velocity of the solid which is related to the normal gradient of the acoustic pressure. Such form of coupling is commonly referred to as *weak coupling*; see also [9, Ch. 1].

#### 4 Extension of the automatic $hp$ -adaptive discretization to coupled acoustics-elasticity problems

To obtain an accurate solution often requires a discretization that is *locally* refined to resolve particular features of the solution. However, such local refinements are often not supported by conventional discretization methods, such as finite differences for instance, and global refinements are generally uneconomical and expensive. To overcome this problem while retaining computational efficiency, we utilize our  $hp$ -adaptive finite-element discretization; for details see [7,8,9]. Our method is capable of adapting the discretization in terms of mesh size,  $h$ , and polynomial approximation order,  $p$ , according to the local resolution requirements of the solution. In regions where the solution varies smoothly,  $p$ -refinement is more effective than  $h$ -refinement to increase the accuracy of the approximation. Conversely, if the solution is non-smooth,  $h$ -refinement is more effective than  $p$ -refinement. To decide where and how to refine (in  $h$  or  $p$ ), we construct an approximation to the discretization-error function as follows: Given an initial grid (the “*coarse grid*”), we construct a corresponding *fine grid* that we obtain by refining the coarse grid uniformly in  $h$  and  $p$ . The solution on the fine grid serves as reference solution to estimate the discretization error in the coarse-grid solution and to construct the next adaptively-refined coarse grid, and so forth. Note that, upon convergence, it is the fine-grid solution rather than the coarse-grid solution that is delivered as final solution. This *two-grid paradigm* forms a central component of our mesh-adaptation strategy. In particular, it renders the adaptivity automatic, i.e. no interaction with the user is required.

Automatic adaptivity releases the user from the burden of designing a mesh that warrants a sufficiently accurate solution. Our algorithm automatically detects changes in the solution behavior induced by material discontinuities and sources, and adapts the discretization to the local resolution requirements. Automatic adaptivity is particularly useful for enhancing the performance of the PML that is commonly used for the truncation of the computational domain, see [4]. To avoid non-physical reflections, an accurate solution within the PML is indispensable. This is corroborated by the fact that the PML is reflectionless only on the continuum level, i.e. as the discrete solution converges to the continuum solution. An accurate solution in the PML is commonly sought after by adjusting the PML damping profile to the specific problem and discretization, typically resulting in non-trivial parameter tuning. By contrast, our automatic adaptivity adapts the discretization to an arbitrary damping profile to any user-specified discretization-error tolerance. This practically eliminates reflections from the truncation of the computational domain without parameter tuning and, hence, renders the application of the PML straightforward; see Section 5 and, in particular, Figs. 3-5, and also Ref. [14].

The work reported on in this paper constitutes the first application of automatic *hp*-adaptivity to coupled multi-physics problems. That is, scalar-valued acoustics and vector-valued elasticity subdomains as well as their interface are treated within the same adaptive framework. To this end, we have enhanced our algorithm for automatic *hp*-adaptivity with the capabilities of propagating refinements through the fluid-solid interface as well as supporting hanging nodes on the interface. Moreover, to achieve refinements that are well balanced between acoustics and elasticity subdomains requires a suitable rescaling of the energy norms in acoustic fluid, elastic formation and elastic tool.

Finally, note that it is actually the solution at the receivers recording the waveforms that we are interested in rather than the solution over the entire domain. Accordingly, accuracy in the domain other than the receiver locations is important only to the extent that it is relevant for the accuracy of our goal functional, i.e. the solution at the receivers. From this viewpoint, a goal-oriented adaptive strategy would be more suited for this type of objective than one that minimizes the energy error over the entire domain; see, e.g., Refs. [16,19] for details on goal-oriented adaptivity. However, preliminary investigations have indicated that for the problem under consideration both adaptive strategies deliver very similar results and, therefore, we base our adaptive strategy on minimizing the energy error over the entire domain.

## 5 Numerical results: benchmarks

### 5.1 Computational setup of the test cases

To validate our computational framework, we consider various problem settings that have been documented in Ref. [6] and compare our results to the reference. In particular, we investigate a setting without the presence of the logging tool (a so-called “*open borehole*”) and a borehole with logging tool; see Fig. 1 for geometry and dimensions. In either setting, the borehole radius is 0.108 m. The radius of the logging tool, if present, is 0.045 m. The source excitation is applied over an area of  $0.004 \text{ m} \times 0.004 \text{ m}$  centered at the location  $(r,z) = (0.102 \text{ m}, 0.0 \text{ m})$ , and the receivers lie on the same radial coordinate as the source. The positions of and the spacing between receivers have been inferred from Ref. [6]. The first receiver has an offset of 3 m from the source. With a receiver spacing of 0.15 m and eight receivers in total, the eighth receiver has an offset of 4.05 m from the source. Note that for comparison with Ref. [6], we shall likewise assume the receivers to be below the source, contrary to what is commonly done. We excite wave propagation with monopole and dipole sources, respectively. The source is a pressure source in the fluid column of the borehole in conformity with Ref. [6], and the receivers record

pressure. Regarding the modeling of the pressure source, we remark that the acoustics Neumann boundary condition  $(21)_1$  applied on a circle with radius  $\varepsilon$  reduces to a point source as  $\varepsilon \rightarrow 0$ . In our computations, we model such a point source as a source with a finite but sufficiently small area as specified above. Note that while the geometry of the problem setting is assumed to be axisymmetric with respect to the borehole axis, the load data may exhibit a specific dependence on the angle of azimuth, as is the case for the dipole source excitation (see Section 2.2 for details).

The domains of borehole fluid, formation and tool are assumed to extend to infinity. To model such an infinite domain, we encompass the computational domain by a Perfectly Matched Layer with a thickness of  $\delta = 0.5$  m. For both acoustics and elasticity subsystems the analytic continuations  $R(r, \omega)$  and  $Z(z, \omega)$  used for complex-coordinate stretching according to Eq. (12) are of the following form:

$$R(r, \omega) = \begin{cases} r & 0 \leq r < r' \\ r + |\eta|b(r)r - i\eta b(r)r & r \geq r' \end{cases}, \quad (50)$$

$$Z(z, \omega) = \begin{cases} z + |\eta_1|b_1(z)z - i\eta_1 b_1(z)z & z \leq z'_1 \\ z & z'_1 < z < z'_2 \\ z + |\eta_2|b_2(z)z - i\eta_2 b_2(z)z & z \geq z'_2 \end{cases}, \quad (51)$$

where

$$b(r) = \left(\frac{r - r'}{0.5\delta}\right)^6, \quad b_1(z) = \left(\frac{z'_1 - z}{0.5\delta}\right)^6, \quad b_2(z) = \left(\frac{z - z'_2}{0.5\delta}\right)^6, \quad (52a)$$

$$\eta = \frac{1}{k(r' + \delta)}, \quad \eta_1 = \frac{1}{k|z'_1 - \delta|}, \quad \eta_2 = \frac{1}{k(z'_2 + \delta)}, \quad (52b)$$

for a given  $k = \omega/V_p$  with  $V_p$  the compressional wave speed in the fluid or solid under consideration (for the compressional wave speed in the solid see Eq. (55) below). In the equations above,  $r' > 0$ ,  $z'_1 < 0$  and  $z'_2 > 0$  denote the coordinates where the “domain of interest” ends and the PML begins. For the cases under consideration, we set  $r' = 1.5$  m,  $z'_1 = -4.5$  m and  $z'_2 = 0.6$  m. Note that it is the scaling of the stretching formulas by the frequency-dependent terms  $\eta$ ,  $\eta_1$  and  $\eta_2$  that renders the decay rate of the numerical solution in the PML essentially independent of the particular frequency under consideration. The complex-coordinate stretching given by Eqs. (50)-(52) ensures that the solution in the PML decays so fast that the PML can be truncated by a homogeneous Dirichlet boundary condition without causing any significant reflections (see Section 2.3 and Ref. [14] for details on the PML).

Throughout, the excitation  $p_{\text{ex}}$  in conformity with Eq. (7) is provided in the

form of a Ricker wavelet which decays rapidly in the time and frequency domains; see Fig. 2 and also Ref. [22]. This has the advantage of confining the frequency spectrum and, thus, the number of frequencies for which computations need to be carried out. The time-dependent excitation is given by

$$p_{\text{R}}(\tau) = A(1 - 2\tau^2)e^{-\tau^2}, \quad (53)$$

where  $A$  is the amplitude,  $\tau := (t - t_s)/t_0$  with  $t_s$  the time at which the maximum occurs and  $\pi t_0$  the characteristic period of the wavelet. Fourier transform of (53) yields the frequency spectrum

$$\hat{p}_{\text{R}}(\omega) = A \left( 2\sqrt{\pi}t_0 e^{-i\omega t_s} \right) \Omega^2 e^{-\Omega^2}, \quad (54)$$

where  $\Omega = \omega t_0/2$ . In our computations, we set  $A = 1$ , which essentially corresponds to normalizing the pressure by some reference pressure, thus rendering  $p_{\text{R}}$  dimensionless. Moreover, a center frequency of approximately 8 kHz is obtained by setting  $t_s = 180 \mu\text{s}$  and  $t_0 = 37 \mu\text{s}$ . At the center frequency of 8 kHz, the wavelength of a compressional wave in the formation is 0.381 m. Unless specified otherwise, the Ricker wavelet is applied as a pressure-source term in the acoustics equations. In conformity with Ref. [6], this pressure source enters the acoustics equation with a negative sign.

Table 1 specifies the material properties of borehole fluid, formation, and logging tool. In subsurface exploration it is customary to specify the material parameters in terms of compressional and shear wave speeds denoted by  $V_p$  and  $V_s$ , respectively. Since the borehole fluid is assumed to be inviscid, it does not support shear waves and, thus,  $V_s^{\text{f}} = 0$  m/s. The compressional wave speed of the fluid,  $V_p^{\text{f}}$ , equals the speed of sound  $c$ ; see Section 3.1. For an elastic solid, the relation between the wave speeds  $V_p^{\text{s}}$  and  $V_s^{\text{s}}$  and the Lamé constants  $\lambda$  and  $\mu$  as introduced in Eq. (33) is given by

$$V_p^{\text{s}} = \left( \frac{\lambda + 2\mu}{\rho_{\text{s}}} \right)^{1/2}, \quad V_s^{\text{s}} = \left( \frac{\mu}{\rho_{\text{s}}} \right)^{1/2}. \quad (55)$$

	$V_p$ [m/s]	$V_s$ [m/s]	$\rho$ [kg/m <sup>3</sup> ]
fluid	1524	0	1100
formation	3048	1793	2200
tool	5860	3130	7800

Table 1

Material properties of borehole fluid, formation and logging tool. Fluid and formation parameters are chosen according to [6]. Since tool parameters are not explicitly given in [6], they have been taken from [24].

The computations are carried out in the frequency domain and subsequently transformed into the time domain as explained in Section 2.1. Choosing a

frequency range of  $[-\hat{f}, \hat{f}] = [-25000 \text{ Hz}, 25000 \text{ Hz}]$  and a frequency spacing of  $\Delta f = 50 \text{ Hz}$ , we determine the frequency-domain solution for the following frequencies:

$$f_j = -\hat{f} + j\Delta f, \quad j = 0, \dots, N, \quad (56)$$

where  $N = 2\hat{f}/\Delta f$ . Considering 1001 frequencies with a spacing of  $\Delta f = 50 \text{ Hz}$ , the time period covered by the inverse Fourier transform is  $1/\Delta f$ , i.e. 0.02 s in our case. We have verified that the chosen frequency spacing is sufficiently fine as is evidenced by the fact that our numerical results reported below remain unchanged under a refinement of the frequency spacing from 50 Hz to 25 Hz. Noting that the following relation holds for the phasor of the complex solution:

$$(\hat{\mathbf{u}}, \hat{p})(\mathbf{x}, -f) = (\overline{\hat{\mathbf{u}}}, \overline{\hat{p}})(\mathbf{x}, f), \quad (57)$$

with the overbar denoting the complex conjugate, it suffices to compute the solution for positive frequencies only. The solution for a negative frequency can then be obtained straightforwardly from the one for the corresponding positive frequency according to Eq. (57).

Starting from a coarse initial mesh and using automatic *hp*-adaptivity, we generate *hp*-refined meshes with less than 3% relative error in the coarse-grid solution measured with the fine-grid solution used as a reference; see Section 4 for details. We generate such meshes for frequencies of 2 kHz, 4 kHz, 6 kHz,  $\dots$ , 26 kHz, where we “roll final meshes forward”, i.e. the final mesh obtained for 2 kHz serves as the initial mesh for 4 kHz, the final mesh obtained for 4 kHz serves as the initial mesh for 6 kHz, and so forth. These 13 meshes are then used to compute the solution for frequencies up to the mesh-specific frequency as follows: the mesh generated for 2000 Hz is used to compute the solution at frequencies of 50 Hz, 100 Hz, 150 Hz,  $\dots$ , 2000 Hz; likewise the mesh generated for 4000 Hz is used to compute the solution at frequencies of 2050 Hz, 2100 Hz, 2150 Hz,  $\dots$ , 4000 Hz; and so forth. Such a procedure guarantees a high level of accuracy while at the same time maintaining computational efficiency. All computations are carried out using the solver MUMPS [21].

## 5.2 Monopole source in an open borehole setting

Before investigating the waveforms in the time domain, let us take a brief look at the convergence behavior of the adaptive algorithm and the solution in the frequency domain from which the time-domain result is derived. Fig. 3 shows the convergence curves of the adaptive algorithm to generate optimal *hp*-meshes for frequencies of 2 kHz, 4 kHz,  $\dots$ , 26 kHz, where in the adaptive process final meshes have been rolled forward as initial meshes at the subsequent frequency as explained in the previous subsection. These curves result from plotting the discretization error against the number of degrees-of-freedom  $N_{\text{dof}}$  in the algebraic scale  $N_{\text{dof}}^{1/3}$ . The fact that the curves yield

approximately straight lines indicates exponential convergence of the discrete solution of the coupled acoustics-elasticity system. The tolerance for the discretization error has been set to 3% in the coarse-grid solution with respect to the fine-grid solution used as a reference. Fig. 3 exhibits that, to meet this error tolerance, for a frequency of 2 kHz it takes a (coarse) grid with about 13k degrees-of-freedom, while for a frequency of 26 kHz a grid with 260k degrees-of-freedom is necessary. However, upon convergence to the optimal *hp*-mesh for a given frequency, it makes sense to use the finest mesh available for accuracy and efficiency purposes. Therefore, we compute the solution on the final fine grid of the respective frequency rather than on the final coarse grid. In general, the discretization error in the fine-grid solution can be expected to be approximately an order of magnitude smaller than the one in the coarse-grid solution. Thus, the final fine grid provides a highly accurate solution both in the domain of interest and in the PML. Such accurate solution in the PML essentially prevents reflections from the truncation of the domain, as is also evidenced by the solution plots discussed in the sequel.

Figs. 4 and 5 show, for exemplification, meshes and solutions, respectively, for the acoustic borehole fluid and the elastic formation in the absence of a tool at the center frequency of the Ricker wavelet,  $f = 8$  kHz. Fig. 4 shows that the *hp*-meshes have been refined to optimally resolve the wave propagation, and the mesh structure clearly reflects this. Refinements have been carried out to capture the wave patterns in acoustic and elastic subdomains as well as the rapid decay of the solution in the PML, thereby highlighting the benefit of our automatic *hp*-adaptive refinement strategy. Compatibility of the meshes on either side of the acoustics-elasticity interface has been achieved by enabling the propagation of refinements through the interface although our algorithm does allow for hanging nodes on the interface. The solution in Fig. 5 shows the different character of the wave propagation in borehole fluid, along the interface and in the formation. In the borehole fluid, waves primarily propagate in the vertical direction, which suggests that the borehole essentially acts as a waveguide in the low and medium frequency range, resulting in quasi one-dimensional wave propagation, whereas in the formation we observe both interface and body waves. Moreover, Fig. 5 shows how, at the interface, the acoustic pressure gradient couples with the normal (here, radial) elastic displacement in accordance with the interface condition given by Eq. (48)<sub>1</sub>.

Fig. 6 shows the time signal and the frequency spectrum for a single receiver at a distance of 3.3 m from the source for a monopole and an open borehole setting. Note that, despite the frequency spectrum of the source excitation by means of a Ricker wavelet is very “smooth” (see Fig. 2), the real and imaginary part of the frequency spectrum of the system response plotted in Fig. 6 are highly oscillatory and, thus, sufficiently many frequency samples are required for an accurate representation of the signal in the time domain.

We verified that the employed frequency spacing of 50 Hz is sufficiently fine for this test case to yield time-domain results that do not change under a further refinement of frequency spacing. In analogy to Fig. 6 (*top*), Fig. 7 shows the time signals and frequency spectra for an array of receivers. Due to the different propagation speeds of the respective waves, the compressional wave arrives first at a given receiver, followed by the shear wave and finally the interface guided waves, i.e. the Stoneley and pseudo-Rayleigh waves; see Refs. [17] and [23] for a description of the different types of waves. As is evidenced in these figures by the amplitude of the respective waves, most of the energy is contained in the Stoneley wave, while only little energy is carried in the shear wave, and the compressional wave contains so little energy that it is hardly visible in that scale. Our results are in good agreement with those obtained in Ref. [6] both in terms of arrival times and shape of the waveform. A close look at Fig. 6 reveals that the difference in arrival times between our results and the ones reported in Ref. [6] is in fact less than 0.1 ms and, for all results reported below, it is consistently the same difference. We attribute the presence of such a small, consistent difference to the fact that the location of our source and receivers matches the ones in Ref. [6] only closely but not exactly, because we inferred these locations from a sketch given in Ref. [6].

Upon comparing our numerical results for the frequency spectra to those presented in Ref. [6], we notice that our spectra are slightly smoother than the ones in the reference, but this difference is really marginal. Note that we solve the problem in the frequency domain and only subsequently transform the solution into the time-domain signal, while Ref. [6] does the converse, i.e. carries out the computations in the time domain and obtains the frequency spectrum subsequently by Fourier transform. Although in theory these two approaches should yield identical results, in practice there may be slight differences due to the time-domain signal not being perfectly smooth and the number of frequencies being finite.

Fig. 8 shows snapshots of the pressure in the borehole fluid and elastic formation at different instances in time<sup>3</sup>, with the elastic pressure being defined as  $p_{\text{elast}} = -\sigma_{ii}/3$  using Einstein summation convention. These snapshots show that the compressional wave in the formation spreads the fastest and, hence, the compressional wave is the first wave to be recorded at the receivers. As can be seen from the plots, the compressional wave is followed by the shear wave and then by the Stoneley wave; compare this figure also to the time signals recorded at the receivers which are plotted in Figs. 6 and 7. The snapshots also convey that the amplitude of the compressional wave is considerably smaller than the one of the subsequent shear wave and Stoneley wave.

<sup>3</sup> An animation corresponding to these snapshots can be found on the following website: <http://www.ices.utexas.edu/centers/aeg/>

### 5.3 Monopole source in the presence of a logging tool

In this subsection, we investigate the effect of the presence of the logging tool on the waveforms recorded at the receiver locations. The tool is modeled as a uniform steel body with material parameters given in Table 1. The tool has a radius of 0.045 m and it is placed in the center of the borehole according to the geometrical description of Fig. 1 (*right*). Note that, in contrast to Ref. [6], we do not model the attenuation streaks of the tool. As pointed out in Section 3.2, for an elasticity problem that is set in a cylindrical coordinate system, finite-energy conditions need in principle to be imposed at radius  $r = 0$  m to cope with the singularity arising from the  $1/r$ -factor in the definition of the strain tensor, Eq. (40). This is the case when an elastic tool in the core of the borehole is present. In practice, though, it turns out that we can get away here with a simple “do-nothing” boundary condition at  $r = 0$  m, the reason being that we do not integrate at  $r = 0$  m, but only at integration points that are close to the vertical axis. The resulting  $1/r$ -factor is then accordingly large and acts like a penalty parameter in the formulation, effectively penalizing the deviation from the finite-energy condition.

Fig. 9 shows the computed waveform for a single receiver at a distance of 3.3 m from the monopole source in the presence of the tool. Upon comparing our waveform to the one given in Ref. [6], we observe that the arrival times of the interface and body waves are in good agreement but that the shape of the interface wave differs. This difference may arise from the fact that we do not model the attenuation streaks of the tool and, thus, the interface wave of the tool may be sufficiently pronounced to alter the time signal that is recorded by the receivers.

Recomputing the same test case subject to the much stronger Dirichlet boundary condition at the source location instead of the standard acoustic-pressure source term, we obtain a waveform that agrees well with Ref. [6] also in terms of the shape of the interface wave; see Fig. 10. We therefore conjecture that the difference in the shape of the interface wave in Fig. 9 when compared to Ref. [6] results from the particular modes of the formation interface wave that the type of source implementation is able to excite in the presence of a non-negligible interface wave of the tool. Regarding Fig. 10, we observe that, similarly to the results without the tool, the Stoneley wave dominates the waveform. However, as was also observed in Ref. [6], the presence of the tool apparently causes a change in the polarity of the Stoneley wave when compared to the open borehole case; compare Fig. 10 to Fig. 6.

#### 5.4 Dipole source in an open borehole setting

We consider the excitation by a dipole source in an open borehole setting, i.e. without the presence of a tool. For a dipole source excitation according to Eqs. (7)-(8), we require the solution components  $(p_1^+; u_{r,1}^+, u_{\theta,1}^+, u_{z,1}^+)$  and  $(p_1^-; u_{r,1}^-, u_{\theta,1}^-, u_{z,1}^-)$  corresponding to the excitation components  $g_1^+$  and  $g_1^-$ , respectively, where the subscript 1 denotes the azimuthal order number  $n = 1$  corresponding to the dipole source. A superposition of the solution components analogous to the one in (8) then yields the solution to the dipole excitation. It turns out that the individual solution components are related as follows:  $(p_1^-; u_{r,1}^-, u_{\theta,1}^-, u_{z,1}^-) = (p_1^+; u_{r,1}^+, -u_{\theta,1}^+, u_{z,1}^+)$ , which can be verified by substitution. Therefore, it suffices to compute the solution component  $(p_1^+; u_{r,1}^+, u_{\theta,1}^+, u_{z,1}^+)$  corresponding to the excitation  $g_1^+$ , and the solution component  $(p_1^-; u_{r,1}^-, u_{\theta,1}^-, u_{z,1}^-)$  corresponding to  $g_1^-$  follows straightforwardly. This effectively reduces the cost associated with the dipole computation by a factor of two.

Figs. 11 and 12 show the time signal and frequency spectrum for a single receiver at a distance of 3.3 m from the source and for an array of receivers, respectively. Fig. 11 displays the flexural interface wave which carries most of the energy and the shear wave; the compressional wave contains so little energy that it is not visible in this scale. For a description of the wave modes excited by a dipole source we refer the reader to Refs. [17,23]. In comparison to the frequency spectrum of the corresponding monopole case (compare Fig. 11 to Fig. 6), we observe that in the dipole case low frequencies are practically not excited. This is due to the low-frequency cutoff of the flexural interface wave; see also Refs. [6] and [23, Ch. 2.5]. Our numerical results compare well in terms of arrival times and shape of the waveform to the ones given in Ref. [6].

Fig. 13 shows snapshots of the pressure in the borehole fluid and elastic formation at different instances in time<sup>4</sup> in the plane given by the azimuthal angle  $\theta = 0^\circ$ . We observe the compressional wave that travels the fastest and is followed by the shear wave and the flexural wave; see also the waveforms in Figs. 11 and 12. From the snapshots it can also be seen that the flexural wave has a much larger amplitude than the compressional wave and the shear wave. Comparing Fig. 13 with Fig. 8 for the corresponding monopole case, we notice that the wave patterns of the respective interface waves, i.e. the Stoneley wave in the monopole case and the flexural wave in the dipole case, are markedly different; compare in particular the respective plots at later instances in time, such as at  $t=1.7$  ms,  $t=2.2$  ms and  $t=2.7$  ms.

<sup>4</sup> An animation corresponding to these snapshots can be found on the following website: <http://www.ices.utexas.edu/centers/aeg/>

### 5.5 Dipole source in the presence of a logging tool

In this subsection, we investigate the excitation in form of a dipole source in the presence of a logging tool. Fig. 14 shows the computed waveform and frequency spectrum at a receiver located 3.3 m from the source. A comparison with Ref. [6] is not possible, since the simulation in the reference was unstable for this case. The frequency spectrum displayed in Fig. 14 exhibits some wiggles that persist under a refinement of the frequency spacing from 50 Hz to 25 Hz as well as under further refinement in space. This indicates that both the frequency spacing and the spatial mesh size are sufficiently fine and do not cause the wiggles in the spectrum.

Fig. 14 conveys that the flexural wave of the formation carries most of the energy. Moreover, when comparing Fig. 14 to the corresponding case without the tool shown in Fig. 11, we notice that the presence of the tool changes the waveform significantly also in the case of a dipole source. A similar observation has been made in Section 5.3 for the monopole case.

## 6 Numerical results: layered formation

In this section, we study coupled acoustics-elasticity wave propagation in the presence of alternating layers of hard and soft formation as depicted in Fig. 15. Such setting is very common in borehole geophysics; see, for instance, Ref. [12]. This problem setting is challenging because of the presence of singularities that arise at points where three different materials meet, as is the case where the interface between hard and soft formation meets the borehole. The presence of singularities renders this problem a challenging case to test our *hp*-adaptive strategy.

Geometry and dimensions of the problem are essentially the same as in Section 5 except for the presence of a layer of hard formation that is located between the vertical coordinates -1 m and -1.5 m and shouldered by two soft formations extending to infinity; see the sketch in Fig. 15. We consider the open borehole setting, i.e. without the tool, and the excitation is provided by means of a monopole source using a pressure source term in form of the Ricker wavelet as detailed in Section 5.1. The positions of source and receivers are identical to the ones specified in Section 5.1.

Table 2 specifies the material properties of borehole fluid and of hard and soft formation. We remark that, in the presence of material layers with interfaces lying in a  $z = \text{const}$  plane, the PML formulation of the elasticity equations as given in Section 3.2 remains valid. This is a consequence of the fact that the

solution remains analytic in terms of the coordinate parallel to the interface; see Ref. [14] for details.

	$V_p$ [m/s]	$V_s$ [m/s]	$\rho$ [kg/m <sup>3</sup> ]
fluid	1524	0	1100
hard formation	3048	1793	2200
soft formation	2300	1000	2000

Table 2

Material properties of borehole fluid and of hard and soft formation for the test case of a layered formation.

In our computations, we choose a frequency range of  $[-\hat{f}, \hat{f}] = [-25000 \text{ Hz}, 25000 \text{ Hz}]$  with a frequency spacing of  $\Delta f = 50 \text{ Hz}$  and subsequently transform the frequency-domain solutions into time-domain signals as described in Section 2.1. While the discretization-error tolerance for the coarse grid has been set to 3%, upon convergence we use the solution obtained on the fine grid which can be expected to have a discretization error that is about one order of magnitude smaller than the one in the coarse-grid solution.

Figs. 16 and 17 show the time signal and frequency spectrum for a single receiver at a distance of 3.3 m from the source and for an array of receivers, respectively. The frequency spectra show pronounced oscillations for frequencies between approximately 0 kHz and 5 kHz and between 10 kHz and 15 kHz. These oscillations persist under refinement of the spatial mesh width and frequency spacing, which suggests that these oscillations are actually physical. This conjecture is further supported by the fact that a computation of this test case using the in-house 2D time-domain finite-difference code from [1] gives very similar results, see Fig. 18. Indeed, the agreement of the respective time signals between our *hp*-adaptive finite-element code using a frequency-to-time-domain transformation and the 2D time-domain finite-difference code is very good both in terms of arrival times and shape of the waveforms.

Regarding the waveforms in Figs. 16 and 17, the time-domain signals exhibit the arrivals of compressional and Stoneley wave only; there is no shear-wave arrival and no pseudo-Rayleigh wave, because the shear-wave speed of the soft formation is smaller than the wave speed of the borehole fluid. Such a formation is also said to be a “slow” formation. Moreover, for a slow formation, the wavetrain generated by the compressional wave is commonly referred to as a “leaky compressional wave”, because it radiates energy into the formation and, thus, attenuates along the borehole; see [23, Ch. 2] and [17, Ch. 5] for details.

## 7 Conclusions

We developed and successfully tested a new *hp*-adaptive finite-element discretization method for the simulation and study of acoustic wave propagation in a fluid-filled borehole coupled with elastic wave propagation in the probed rock formation and in the logging tool. This development constitutes the first application of automatic *hp*-adaptivity to a coupled multi-physics problem, which requires the non-trivial capability of propagating refinements between acoustics and elasticity subdomains through their common interface. A distinct advantage of the combination of *hp*-adaptivity with the Perfectly Matched Layer technique is that it practically eliminates non-physical reflections from the truncation of the computational domain. Computations were carried out in the frequency domain. Using an inverse Fourier transform, the frequency-domain solutions were subsequently transformed into the time domain to produce the waveforms at the receiver positions. To validate our computational framework, we compared our results to published reference data and to results from an in-house finite-difference code, and found very good agreement. Convergence to a user-defined tolerance for the discretization error confirmed the accuracy delivered by our method in the presence of complex geometrical and physical conditions and indicates its potential for the simulation of borehole acoustic measurements.

## Acknowledgments

This work was financially supported by The University of Texas at Austin's *Joint Industry Research Consortium on Formation Evaluation* sponsored by Anadarko, Aramco, Baker Atlas, BHP Billiton, BP, British Gas, Chevron, ConocoPhillips, ENI E&P, ExxonMobil, Halliburton Energy Services, Marathon Oil Corporation, Mexican Institute for Petroleum, Hydro, Occidental Petroleum Corporation, Petrobras, Schlumberger, Shell International E&P, Statoil, Total, and Weatherford International Ltd. Moreover, the first author was supported by a stipend from the Netherlands Organization for Scientific Research (NWO) and by an ICES postdoctoral fellowship from the Institute for Computational Engineering and Sciences (ICES) of The University of Texas at Austin. This support is gratefully acknowledged.

The authors also would like to thank Arthur Cheng, Joakim Blanch, and David Pardo for helpful discussions, Jun Ma and Amir Reza-Rahmani for providing the finite-difference results presented in Section 6, and Jason Kurtz for his help with the solver MUMPS [21].

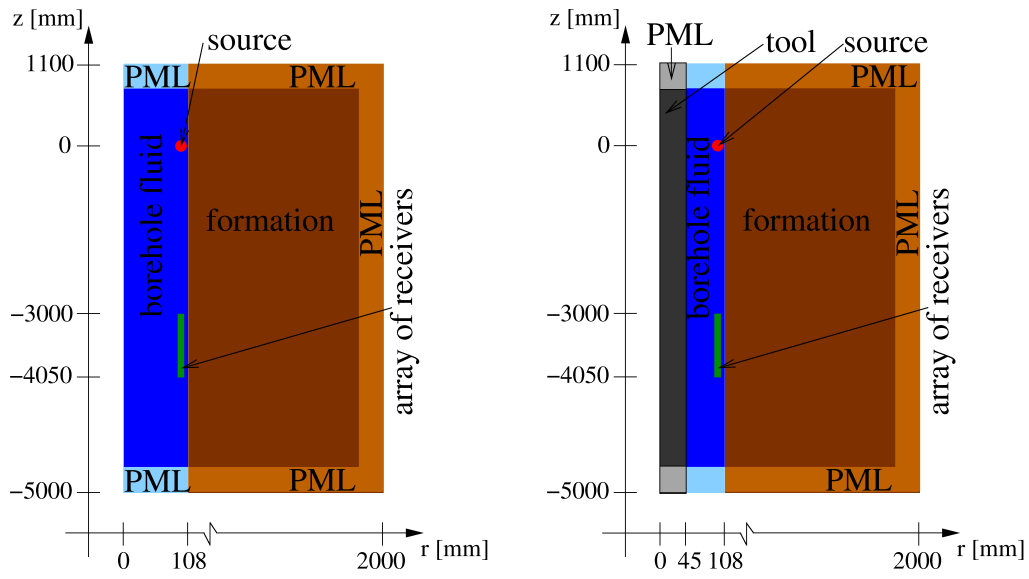


Figure 1. Geometry and dimensions of the computational domain with location of source and receivers according to Ref. [6]. The spacing between receivers is 150 mm, and each PML is 500 mm thick. *Left* : “Open borehole setting” (without logging tool); *right* : setting with logging tool.

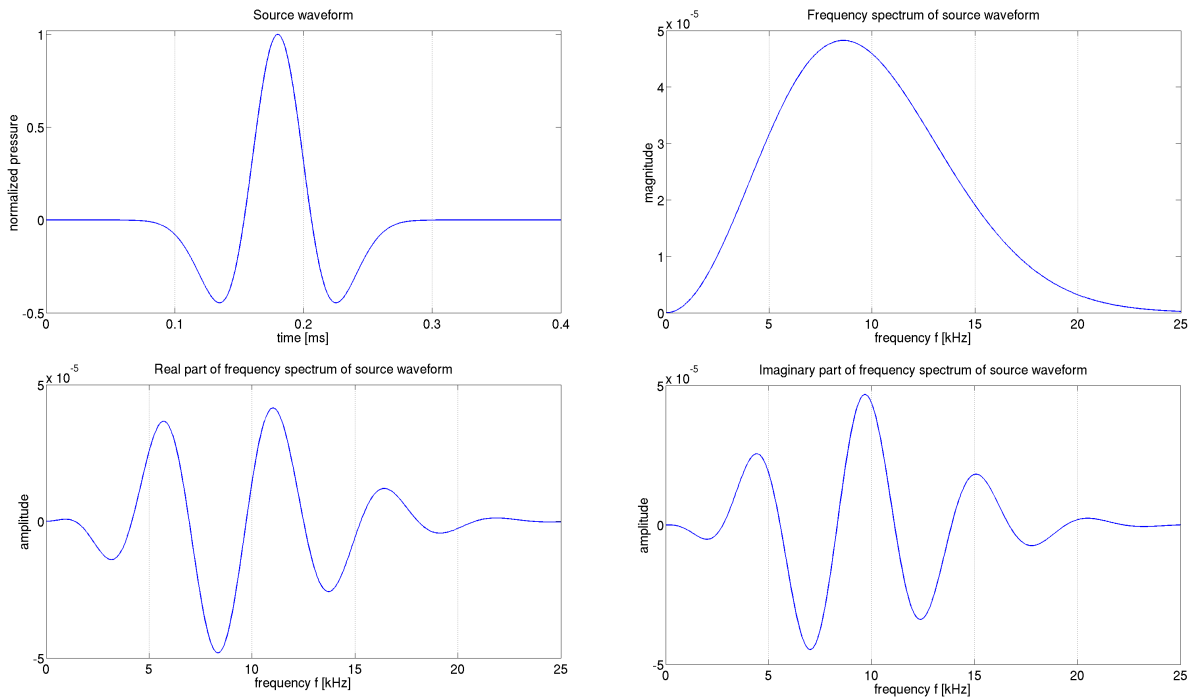


Figure 2. The Ricker wavelet with a center frequency of 8 kHz is used as the source wavelet; time signal (*top left*), magnitude of frequency spectrum (*top right*), and real part (*bottom left*) and imaginary part (*bottom right*) of frequency spectrum.

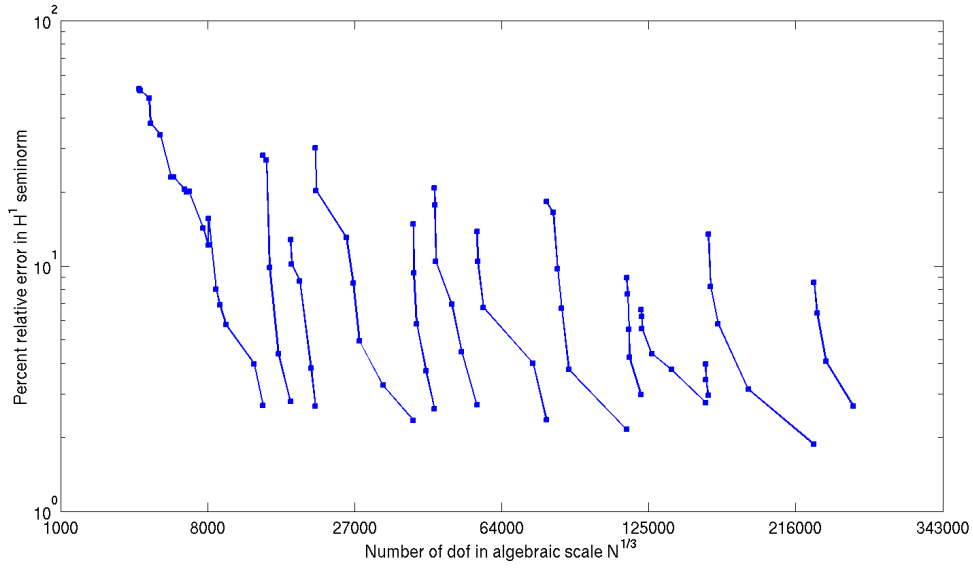


Figure 3. Percent relative discretization error versus number of degrees-of-freedom in the algebraic scale  $N_{\text{dof}}^{1/3}$  for the coarse-grid solution at frequencies of 2 kHz, 4 kHz,  $\dots$ , 26 kHz (curves from left to right), where in the adaptive process final meshes have been rolled forward, i.e. the final coarse mesh obtained for 2 kHz serves as the initial mesh for 4 kHz, and so forth.

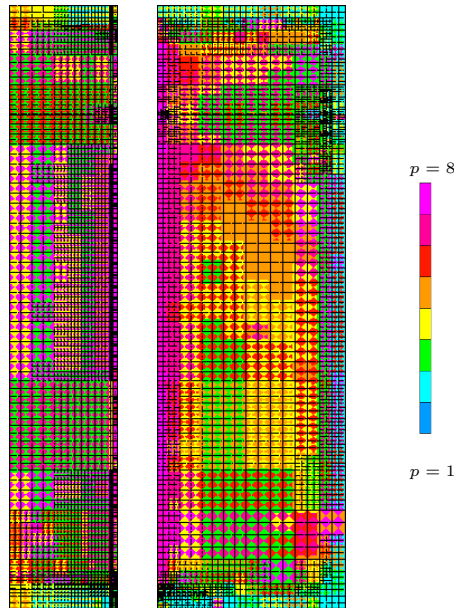


Figure 4. Monopole source in an open borehole setting: Meshes (final fine grids generated by the adaptivity) for the center frequency of 8 kHz; *from left to right*: Acoustics mesh, elasticity mesh and color bar indicating the polynomial approximation order  $p$  of element edges and interiors. Note that for enhanced visibility the acoustics subdomain has been scaled by a factor of 10 in the radial direction.

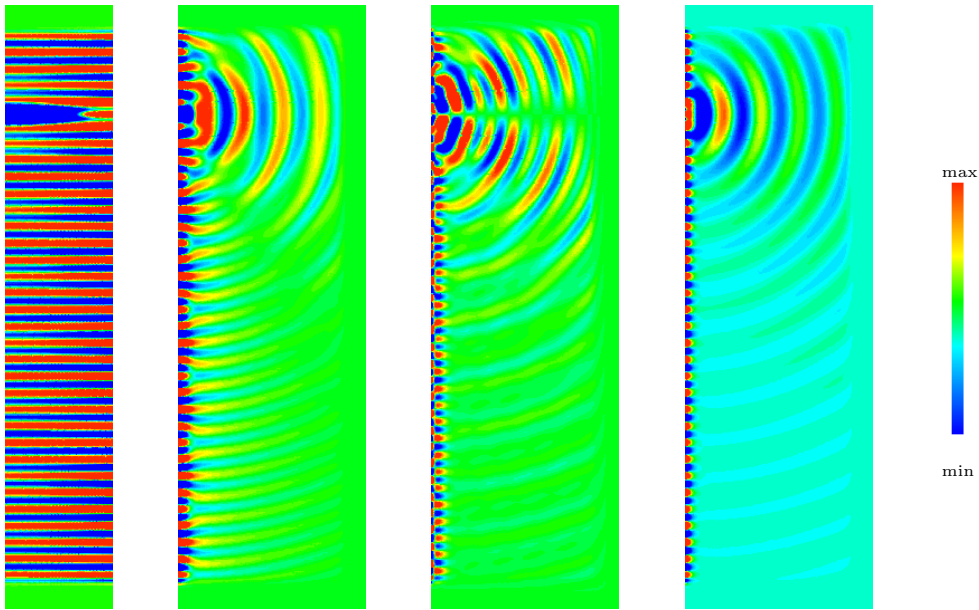


Figure 5. Monopole source in an open borehole setting: Frequency-domain solution at the center frequency of 8 kHz; *from left to right*: Acoustic pressure  $p$ , radial elastic displacement  $u_r$ , vertical elastic displacement  $u_z$ , elastic pressure  $p_{\text{elast}}$  and color bar indicating the range of the solution. Note that for enhanced visibility the acoustics subdomain has been scaled by a factor of 10 in the radial direction. Moreover, for enhanced visibility, the respective plotting ranges have been set to  $[0.1 \text{ min}, 0.1 \text{ max}]$ .

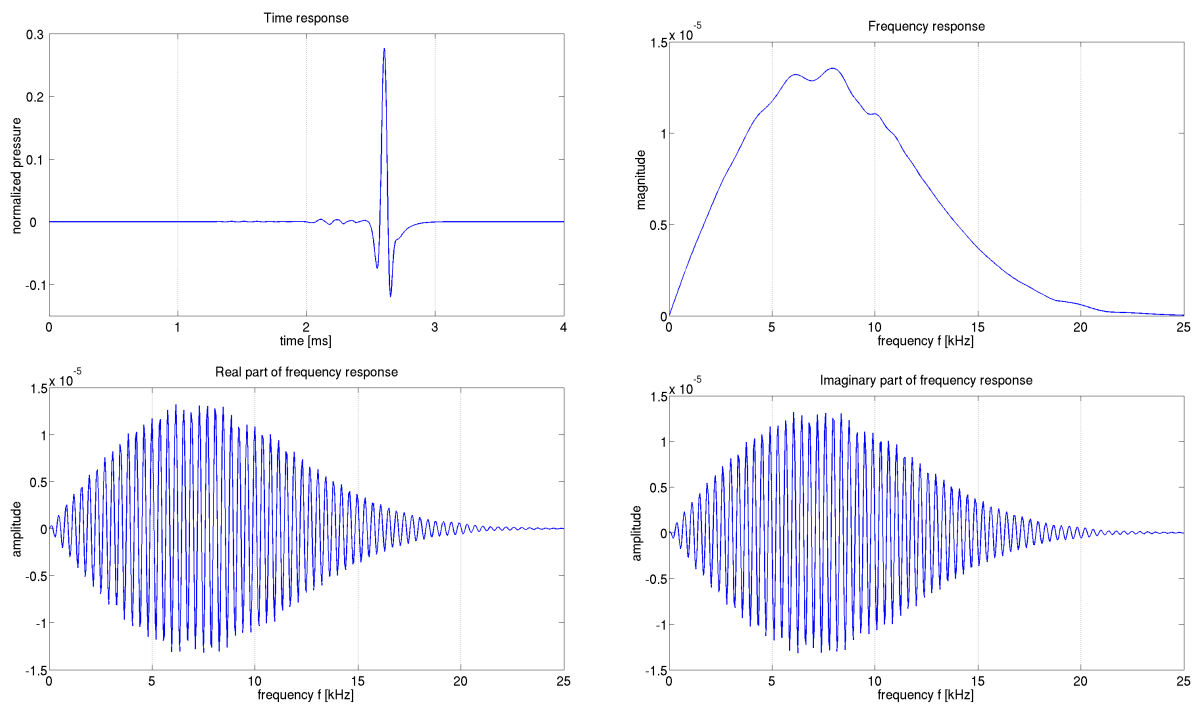


Figure 6. Monopole source in an open borehole setting (no tool): time signal (*top left*), magnitude of frequency spectrum (*top right*), and real part (*bottom left*) and imaginary part (*bottom right*) of frequency spectrum at a receiver with an offset of 3.3 m from the source.

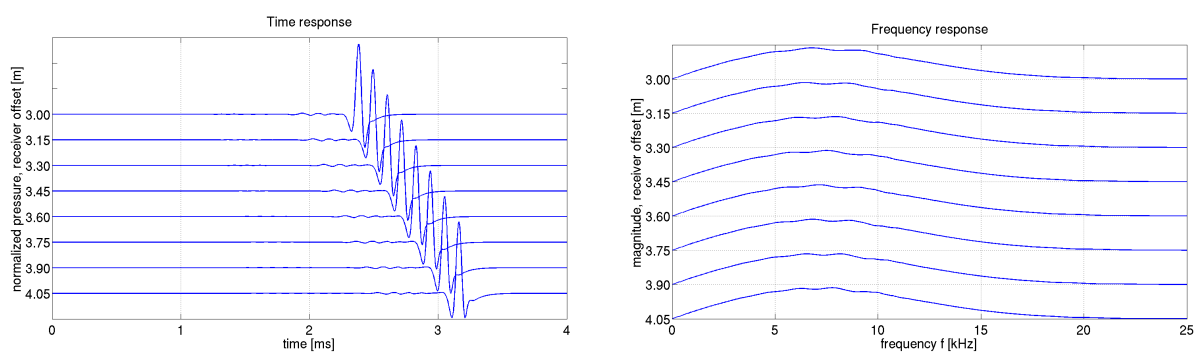


Figure 7. Monopole source in an open borehole setting: time signal (*left*) and frequency spectrum (*right*) at various receiver locations.

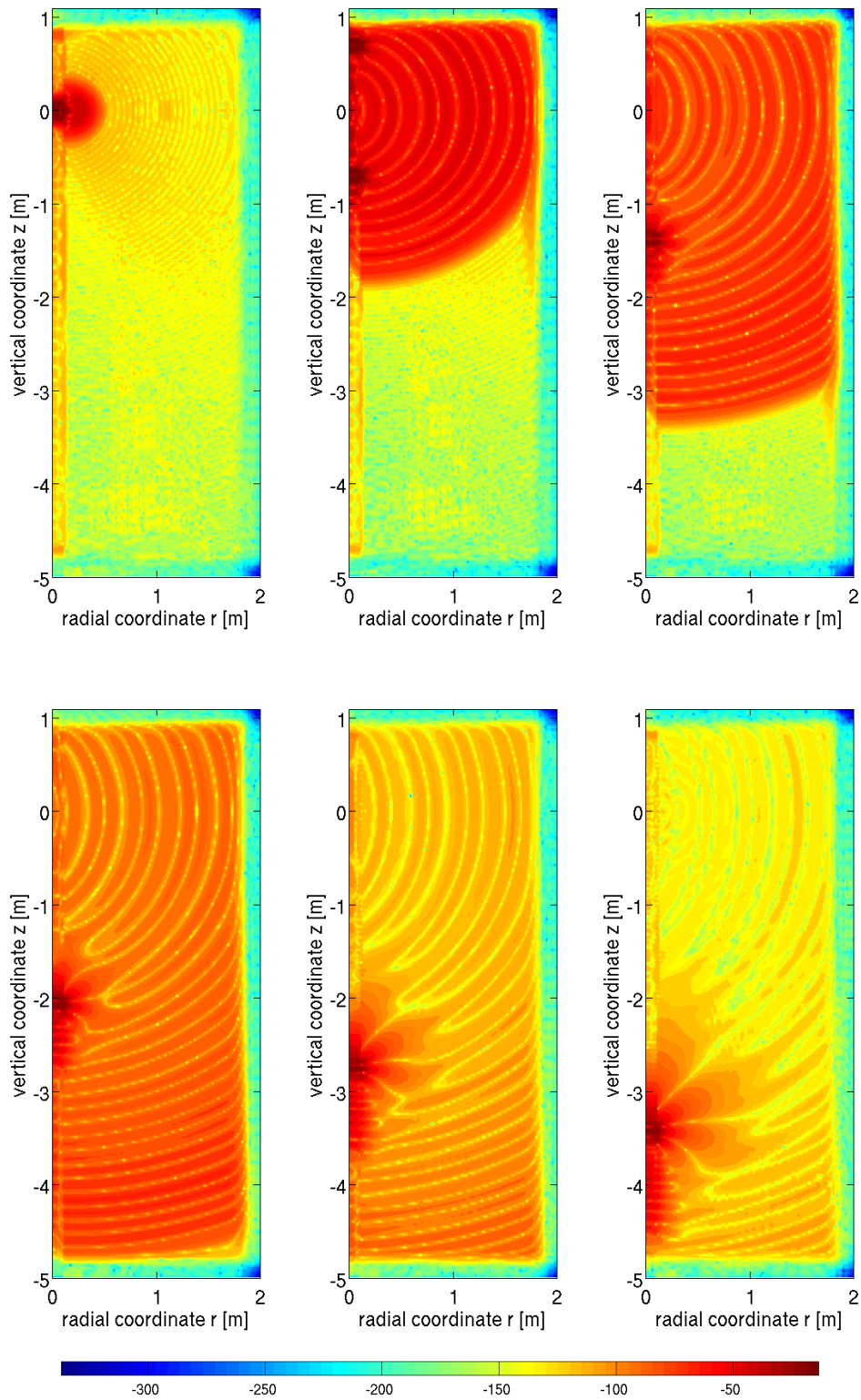


Figure 8. Monopole source in an open borehole setting: Snapshots of the pressure in acoustic borehole fluid and elastic formation at  $t=0.2$  ms (*top left*),  $t=0.7$  ms (*top middle*),  $t=1.2$  ms (*top right*),  $t=1.7$  ms (*bottom left*),  $t=2.2$  ms (*bottom middle*) and  $t=2.7$  ms (*bottom right*). The interface between acoustic borehole fluid and elastic formation is located at  $r = 0.108$  m. The color scale measures pressure in the decibel scale  $20 \log_{10}(|p(\mathbf{x}, t)|)$ .

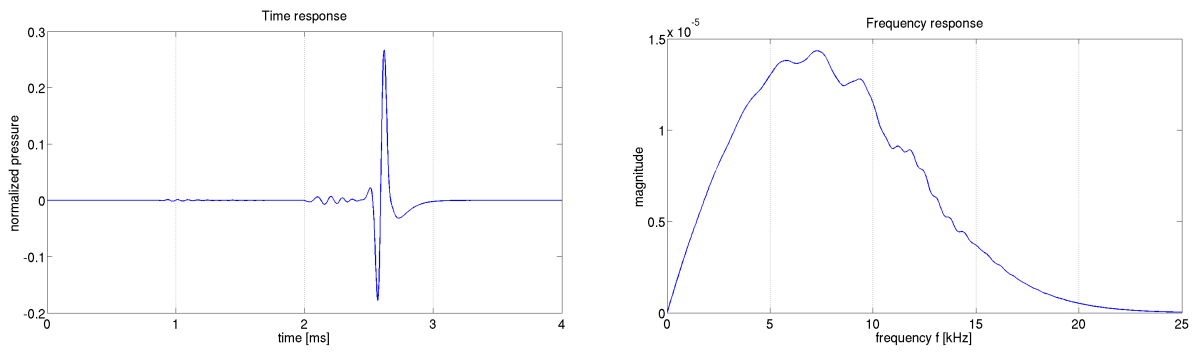


Figure 9. Monopole source in the presence of a logging tool (for a standard source excitation in the form of an acoustic-pressure source term): time signal (*left*) and frequency spectrum (*right*) at a receiver with an offset of 3.3 m from the source.

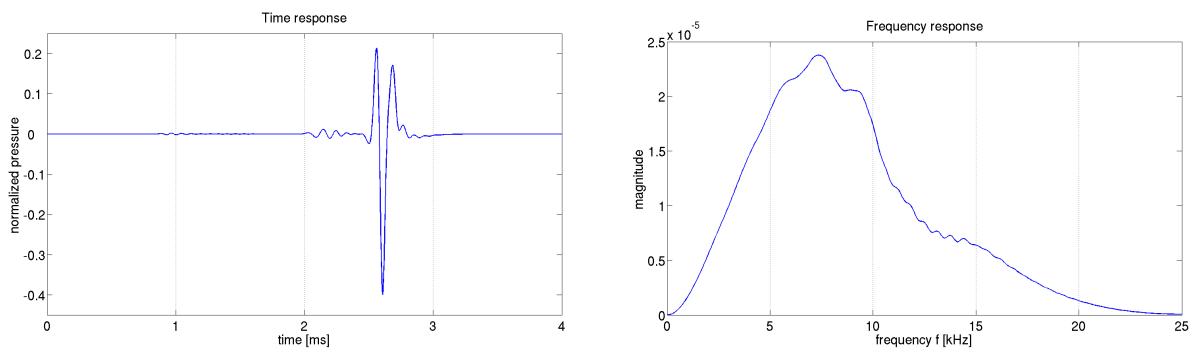


Figure 10. Monopole source in the presence of a logging tool (for a source excitation in the form of a Dirichlet condition): time signal (*left*) and frequency spectrum (*right*) at a receiver with an offset of 3.3 m from the source.

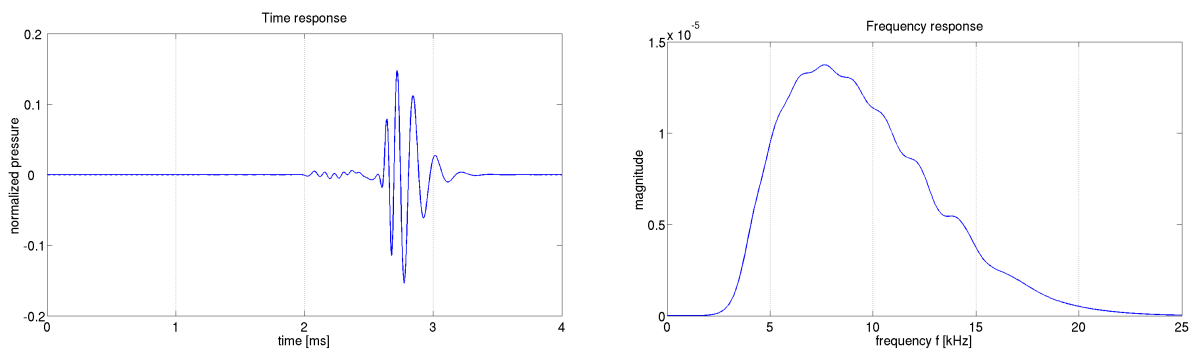


Figure 11. Dipole source in an open borehole setting (no tool): time signal (*left*) and frequency spectrum (*right*) at a receiver with an offset of 3.3 m from the source.

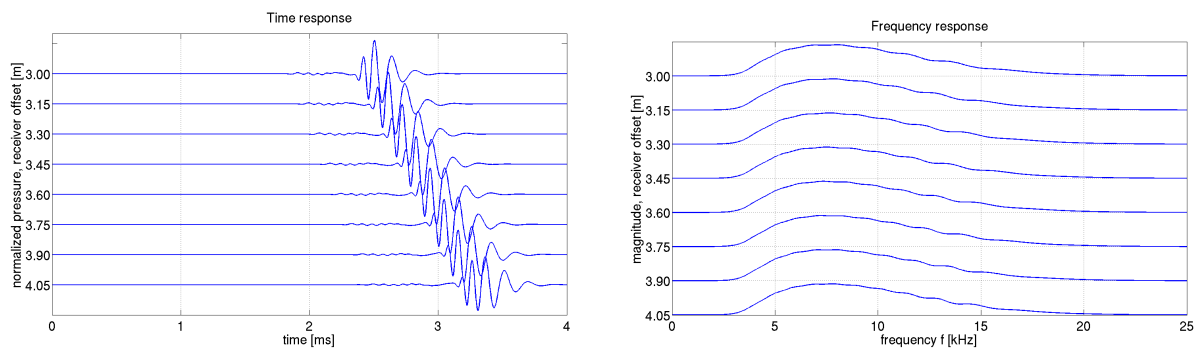


Figure 12. Dipole source in an open borehole setting: time signal (*left*) and frequency spectrum (*right*) at various receiver locations.

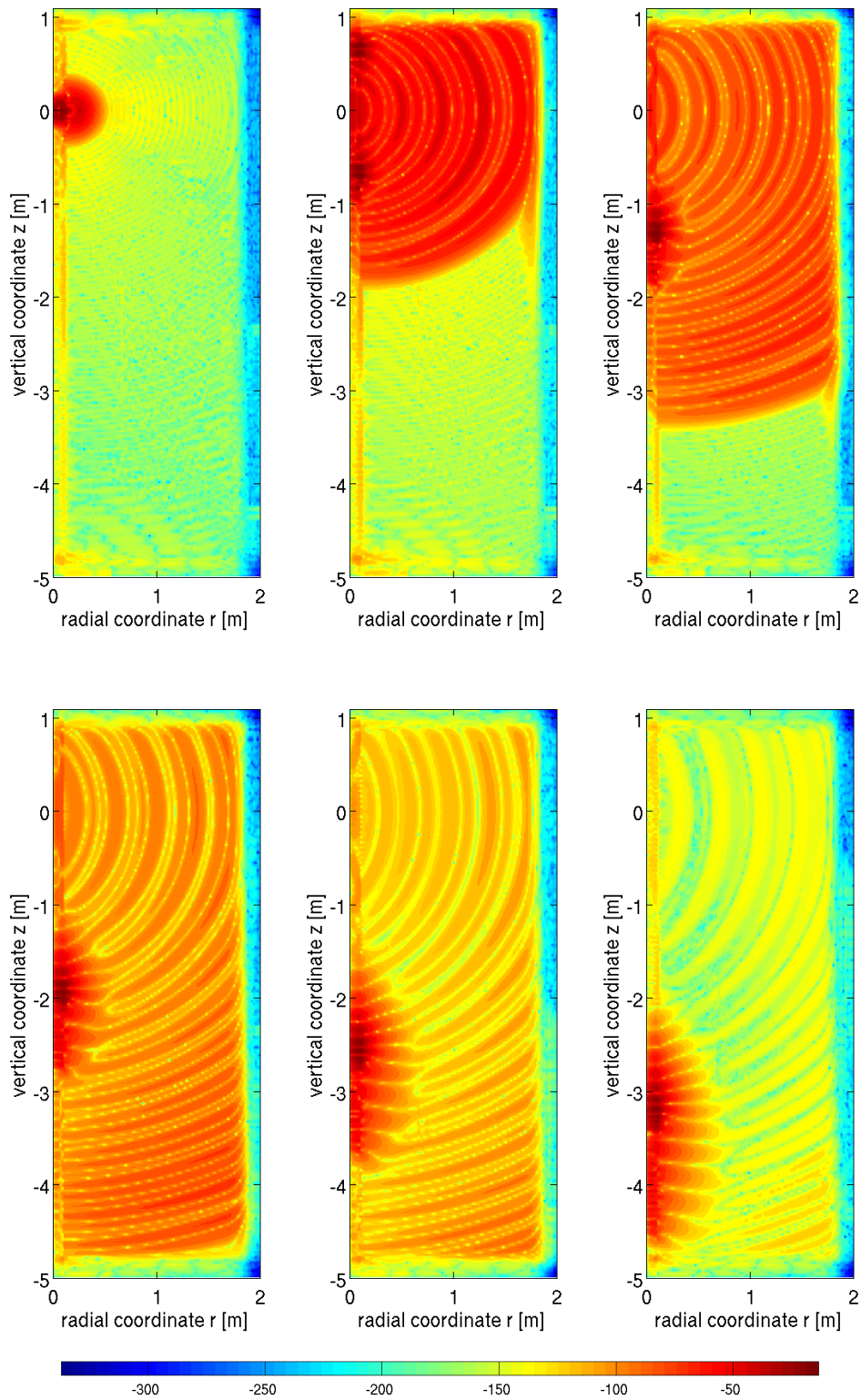


Figure 13. Dipole source in an open borehole setting: Snapshots of the pressure in acoustic borehole fluid and elastic formation at  $t=0.2$  ms (*top left*),  $t=0.7$  ms (*top middle*),  $t=1.2$  ms (*top right*),  $t=1.7$  ms (*bottom left*),  $t=2.2$  ms (*bottom middle*) and  $t=2.7$  ms (*bottom right*). The interface between acoustic borehole fluid and elastic formation is located at  $r = 0.108$  m. The color scale measures pressure in the decibel scale  $20 \log_{10}(|p(\mathbf{x}, t)|)$ .

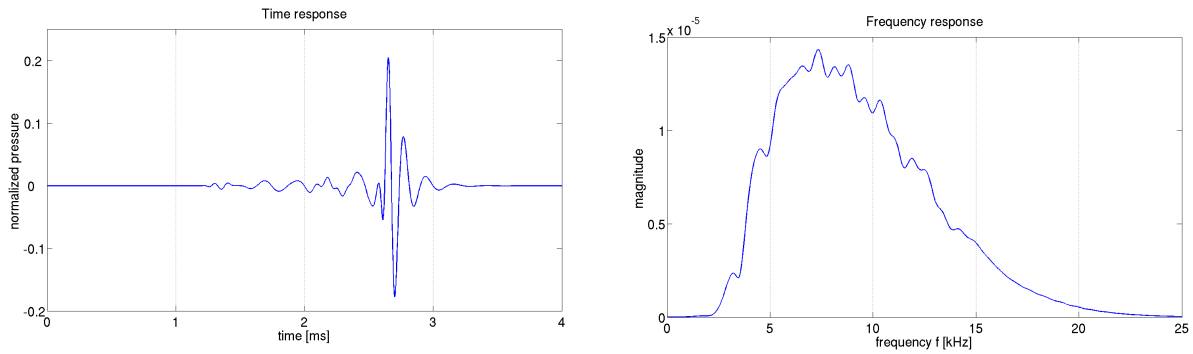


Figure 14. Dipole source in the presence of a logging tool: time signal (*left*) and frequency spectrum (*right*) at a receiver with an offset of 3.3 m from the source.

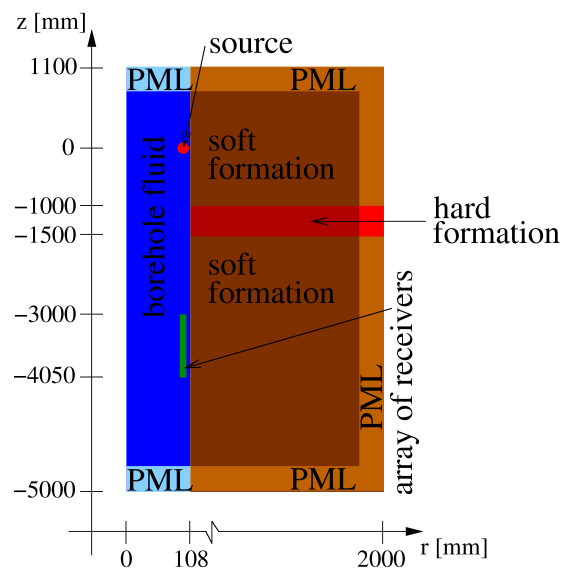


Figure 15. Geometry and dimensions of the computational domain for the layered formation problem. The thickness of the hard-formation layer is 500 mm; the spacing between receivers is 150 mm, and each PML is 500 mm thick.

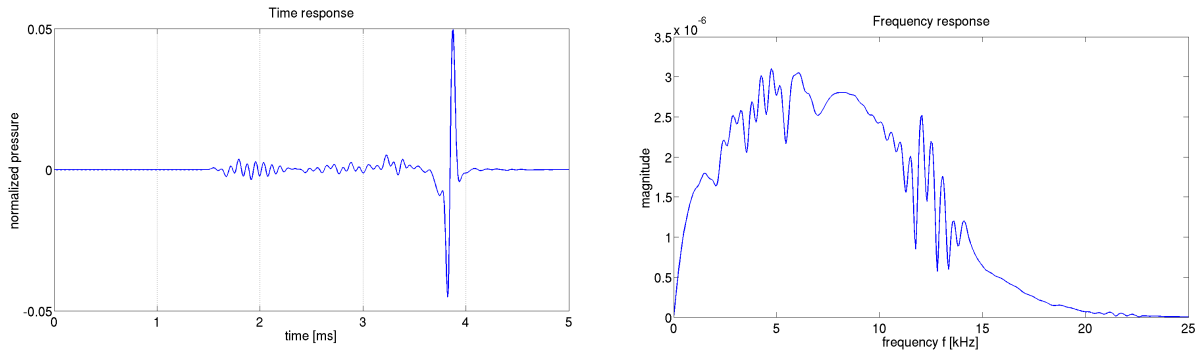


Figure 16. Hard-formation finite-thickness layer shouldered by soft formations extending to infinity with a monopole source in an open borehole setting (no tool): time signal (*left*) and frequency spectrum (*right*) at a receiver with an offset of 3.3 m from the source.

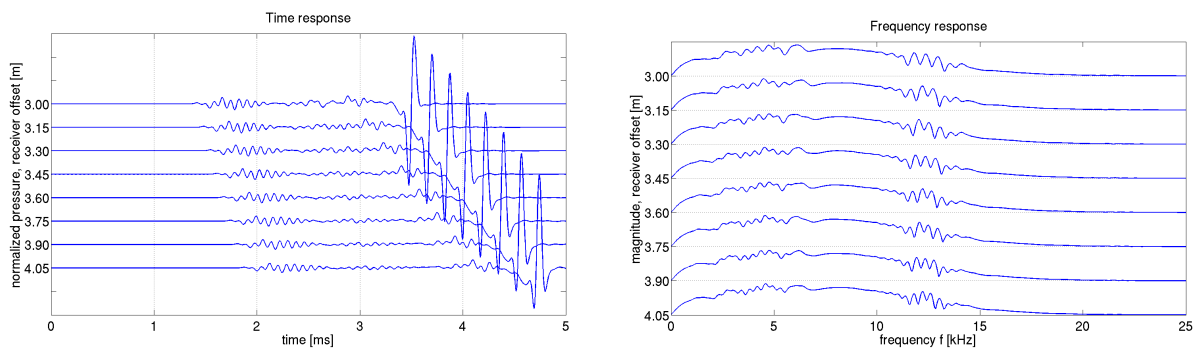


Figure 17. Hard-formation finite-thickness layer shouldered by soft formations extending to infinity with a monopole source in an open borehole setting (no tool): time signal (*left*) and frequency spectrum (*right*) at various receiver locations.

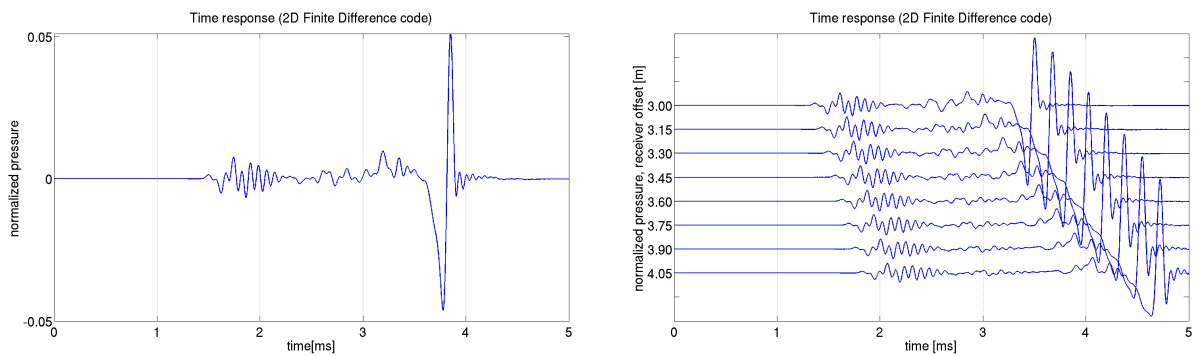


Figure 18. Hard-formation finite-thickness layer shouldered by soft formations extending to infinity with a monopole source in an open borehole setting (no tool); results obtained with a 2D finite-difference code: time signal at a receiver with an offset of 3.3 m from the source (*left*) and at various receiver locations (*right*).

## References

- [1] Borehole Sonic Toolbox, Users Manual, Formation Evaluation Group, Department of Petroleum and Geosystems Engineering, The University of Texas at Austin, U.S.A., 2007.
- [2] F.O. Alpak, C. Torres-Verdín, and T.M. Habashy, *Joint inversion of transient pressure and DC resistivity measurements acquired with in-situ permanent sensors: A numerical study*, *Geophysics* **69** (2004), no. 5, 1173–1191.
- [3] F.O. Alpak, C. Torres-Verdín, and K. Sepehrnooni, *Estimation of axisymmetric spatial distributions of permeability and porosity from pressure-transient data acquired with in situ permanent sensors*, *J. Petroleum Science Engrg.* **44** (2004), no. 3–4, 231–267.
- [4] J.-P. Bérenger, *A perfectly matched layer for the absorption of electromagnetic waves*, *J. Comput. Phys.* **114** (1994), 185–200.
- [5] Y.-H. Chen, W.C. Chew, and Q.-H. Liu, *A three-dimensional finite difference code for the modeling of sonic logging tools*, *J. Acoust. Soc. Am.* **103** (1998), no. 2, 702–712.
- [6] A.C.H. Cheng and J.O. Blanch, *Numerical modeling of elastic wave propagation in a fluid-filled borehole*, *Communications in Computational Physics* **3** (2008), no. 1, 33–51.
- [7] L. Demkowicz, *Fully automatic hp-adaptivity for Maxwell’s equations*, *Comput. Methods Appl. Mech. Engrg.* **194** (2005), 605–624.
- [8] ———, *Computing with hp-adaptive finite elements. I. One- and two-dimensional elliptic and Maxwell problems*, CRC Press, Taylor and Francis, 2006.
- [9] L. Demkowicz, J. Kurtz, D. Pardo, M. Paszyński, W. Rachowicz, and A. Zdunek, *Computing with hp-adaptive finite elements. II. Frontiers: Three-dimensional elliptic and Maxwell problems with applications*, CRC Press, Taylor and Francis, 2007.
- [10] M.C. Junger and D. Feit, *Sound, structures, and their interaction*, The MIT Press, Cambridge, Massachusetts, 1986, 2nd edition.
- [11] C. Lanczos, *Applied analysis*, Dover, 1988.
- [12] Q.-H. Liu, E. Schoen, F. Daube, C. Randall, and P. Lee, *A three-dimensional finite difference simulation of sonic logging*, *J. Acoust. Soc. Am.* **100** (1996), no. 1, 72–79.
- [13] Q.H. Liu and B.K. Sinha, *A 3D cylindrical PML/FDTD method for elastic waves in fluid-filled pressurized boreholes in triaxially stressed formations*, *Geophysics* **68** (2003), no. 5, 1731–1743.

- [14] C. Michler, L. Demkowicz, J. Kurtz, and D. Pardo, *Improving the performance of Perfectly Matched Layers by means of hp-adaptivity*, Numerical Methods for Partial Differential Equations **23** (2007), no. 4, 832–858.
- [15] R. Mittet and R. Lasse, *High-order, finite-difference modeling of multipole logging in formations with anisotropic attenuation and elasticity*, Geophysics **61** (1996), no. 1, 21–33.
- [16] J.T. Oden and S. Prudhomme, *Goal-oriented error estimation and adaptivity for the finite element method*, Computers and Mathematics with Applications **41** (2001), 735–756.
- [17] F.L. Paillet and C.H. Cheng, *Acoustic waves in boreholes*, CRC Press, Boca Raton, 1991.
- [18] D. Pardo, C. Torres-Verdín, M.J. Nam, M. Paszynski, and V. Calo, *Fourier series expansion in a non-orthogonal system of coordinates for the simulation of 3D alternating current borehole resistivity measurements*, Comput. Methods Appl. Mech. Engrg. (under review).
- [19] S. Prudhomme and J.T. Oden, *On goal-oriented error estimation for elliptic problems: application to the control of pointwise errors*, Comput. Methods Appl. Mech. Engrg. **176** (1999), 313–331.
- [20] D.P. Schmitt and M. Bouchon, *Full-wave acoustic logging: synthetic microseismograms and frequency-wavenumber analysis*, Geophysics **50** (1985), no. 11, 1756–1778.
- [21] MUMPS: A MULTifrontal MASSively Parallel sparse direct Solver, <http://graal.ens-lyon.fr/mumps/>.
- [22] A. Tadeu, P.A. Mendes, and J. António, *3D elastic wave propagation modelling in the presence of 2D fluid-filled thin inclusions*, Engineering Analysis with Boundary Elements **30** (2006), 176–193.
- [23] X.-M. Tang and A. Cheng, *Quantitative borehole acoustic methods*, Handbook of geophysical exploration, Seismic exploration (K. Helbig and S. Treitel, eds.), vol. 24, Elsevier, 2004.
- [24] Y. Zheng, X. Huang, and M.N. Toksöz, *A finite element analysis of the effects of tool eccentricity on wave dispersion properties in borehole acoustic logging while drilling*, Proceedings of the 74th Annual Meeting of the Society of Exploration Geophysicists, Denver, CO, 2004.